Crop Classification With Multifrequency Multitemporal Polarimetric and Interferometric SAR Data

Noelia Romero-Puig , *Member, IEEE*, Mario Busquier, Jiayin Luo , *Member, IEEE*, Juan M. Lopez-Sanchez , *Senior Member, IEEE*, Francesca Ticconi, *Member, IEEE*, and Irena Hajnsek , *Fellow, IEEE*

Abstract—The combination of radar-derived features extracted from a dataset formed by multitemporal polarimetric images and interferometric products acquired at various frequency bands has been evaluated for crop classification in this work. Fully polarimetric images acquired by the F-SAR airborne sensor at three frequency bands (L, C, and X) and at three separate dates during the CROPEX14 campaign are exploited for this purpose. The images include consistent repeat-pass acquisitions with different baselines. Results show that all data dimensions contribute to improve the classification accuracy. The main novelty of this work is the joint use of different frequency bands (in groups of two and three) and specific interferometric data suitable for crops (short temporal baselines and large spatial baselines). The achieved performance with different combinations of input features is analyzed both globally and for specific crops. Among other conclusions, L- and X-bands show the best performance of all band pairs. Since they are the most extreme, their complementary sensitivity is maximized when used together.

Index Terms—Crop classification, interferometry, multifrequency, multitemporal, polarimetry, synthetic aperture radar (SAR).

I. INTRODUCTION

SYNTHETIC aperture radar (SAR) sensors provide images that are not limited to intensity or gray-level values, but incorporate additional features, which can be exploited in many applications. In general, these features are grouped into four dimensions or axes: polarimetry, time series, interferometry, and multifrequency. These axes of SAR data diversity can be combined for image classification, since they provide complementary sensitivity to different aspects of the scene. This helps the classification principle (i.e., the identification of different land covers) and, hence, improves the performance of the classifiers. Among all applications of image classification, this study is focused on crop-type mapping or crop classification.

Existing examples of combination of polarimetry, time series, interferometry, and multifrequency for crop classification are reviewed in this section. Table I lists the combinations found in the literature. Particular focus is set on the combination of the different data axes with multifrequency information. Multispectral radar data are potentially useful for classification because different wavelengths provide diversity in penetration depth (e.g., over vegetation) and in the scale or size of the elements of the scene to which the radar is sensitive.

Polarimetry [1] is sensitive to the shape and orientation of the elements that constitute the scene. Therefore, it helps distinguishing crop covers characterized by distinct morphology or geometry. Regarding the use of SAR polarimetry (PolSAR) at multiple frequency bands, the authors in [2], [3], and [4] provide examples comparing the classification performance of various polarimetric modes at different bands. However, only a few studies effectively combined multifrequency data to enhance the classification result. The combination of L-, C-, and X-bands was successfully tested in [5] for general land cover classification using one polarimetric image at each band. In the context of crop-type mapping, L-, C-, and X-bands were also used in [6], whereas P-, L-, and C-bands were combined in [7] and [8], L- and C-bands in [9], [10], [11], [12], and [13], and C- and X-bands in [14]. In all cases, the classification performance improved when multiple bands were employed with respect to single bands, thus corroborating the commented complementary sensitivity as a function of the wavelength.

TABLE I
BIBLIOGRAPHY EXAMPLES OF COMBINATIONS OF POLARIMETRY, TIME SERIES, INTERFEROMETRY, AND MULTIFREQUENCY FOR CROP-TYPE MAPPING

Polarimetry	Time series	Interferometry	Multi-frequency	Publications
X	X			[9], [10], [16], [17], [18]
X		X		[28]
	X	X		[27]
X	X	X		[30]
X			X	[6], [7], [8], [9], [10], [13]
X	X		X	[9], [10], [16], [19], [20]
X	X	X	X	[31]

Time series of satellite images constitute the major source of information for land cover classification nowadays [15]. Regarding crop classification, the crop calendar (sowing–growth–harvest dates) is usually specific of each crop type in the same geographical region, so time series allow separating classes by their temporal patterns. This makes this data axis especially useful in this application domain [16]. The exploitation of time series of polarimetric features for crop classification is also well documented in the literature [9], [10], [16], [17], [18], [19], [20]. Notably, the combination of time series of polarimetric observables acquired at L- and C-bands was evaluated for crop-type mapping in [9] and [10], at L-, C-, and X-bands in [19], and at C- and X-bands in [20]. Tillage mapping was also addressed by combining time series of L-, C-, and X-bands images in [21]. The main conclusion of these studies was that the most relevant axis for this application is time. Crops exhibit specific cultivation calendars and, therefore, their radar responses change with time and differently for each crop species. As a consequence, there are specific dates that serve to separate sets of crops, and this situation changes along time and among crops. In fact, when the observation period covered by the time series includes images acquired before sowing and after harvest, results are usually better than when they are all comprised within the growing season. In addition, the inclusion of two frequency bands was also beneficial for the classification performance.

SAR interferometry (InSAR) [22] is potentially suited for classification of land covers in which there is a vertical distribution of elements, e.g., urban areas and vegetation (forests and crops). The information provided by interferometry takes the form of coherence and phase, both related to the scene properties. In particular, repeat-pass coherence is the interferometric feature most applied in crop classification. Vegetation covers show different decorrelation rates over time, to which the repeat-pass coherence is sensitive. It is therefore sensitive to cultivation practices and to the crop calendar. InSAR products derived from ERS-1 and ERS-2 data were first employed for land cover classification in [23] and [24]. These pioneering works showed clearly that there is more information content in the time series of the interferometric coherence than in the backscatter intensity. Much more recently, thanks to the availability of long time series of Sentinel-1 images, more complete results have been obtained by [25] and [26]. They demonstrate the contribution of repeat-pass coherence for land cover mapping, its complementarity with respect to backscatter intensity, and, moreover, the independence of this contribution with respect to the classifier. In addition, the two available polarimetric channels (VV and VH)

provide different information, also complementing the potential of this information source for classification. In the same line, the usefulness of time series of six-day Sentinel-1 interferometric coherence for crop-type mapping was demonstrated in [27].

Single-pass interferometry, which is sensitive to the vertical distribution of the elements in the scene, has been recently exploited for crop-type mapping in [28] using TanDEM-X data. Volume decorrelation makes tall crops produce lower coherence levels than short crops, so this feature was found very helpful in this application. Moreover, when time series of single-pass acquisitions are available, one can also generate repeat-pass interferograms with images of different dates, hence increasing the sensitivity to scene properties.

As for the combination of polarimetry and interferometry (i.e., PolInSAR [29]) for crop-type mapping, the TanDEM-X data employed in [28] were acquired in dual-pol mode. Thus, time series of single-pass coherences at HH and VV channels were used and combined. Later on, additional PolInSAR features derived from the same dataset were employed for crop classification in [30]. The results proved the complementarity between PolSAR and PolInSAR observables, which provide the highest classification accuracy when exploited jointly.

Finally, time series of dual-pol satellite images acquired at L-, C-, and X-bands have been recently combined in [31] for crop-type mapping. Different scenarios were evaluated, including combinations of two or three bands, using either the whole time series or a subset limited to the number of images for the band with the fewest observations. However, the lack of overlapping polarimetric combinations across frequencies limited the study to the use of only repeat-pass interferometric coherences and backscattering coefficients of individual channels as input features.

From this review, one concludes that the use of multiple frequency bands has not been fully explored yet, especially when considering its combination with interferometry and PolInSAR, and only in a limited way with time series. In addition, the exploitation of PolInSAR data for crop classification, even at a single frequency, and both at single dates or in time series, is clearly not sufficiently studied. In this work, these two aspects are analyzed in detail through the following questions.

1) Do all SAR data axes (time, polarimetry, interferometry, and multifrequency) contribute to crop classification, both alone and in combination?
2) Is the combination of multiple frequency bands beneficial for crop classification using polarimetric and

interferometric features? If yes, which sets of frequency bands perform best?

3) Which specific configurations contribute most to crop classification? and how could they be exploited with current or future satellite systems?

To answer these questions, an exhaustive analysis of the results obtained with a well-known machine learning classifier [random forest (RF)] is carried out by using different sets of input features and measuring the performance at overall and crop-specific levels. Other state-of-the-art classification methods could have been employed too, like deep learning models, such as convolutional neural networks and transformers. However, the focus of this work is placed on the feature sets used as inputs for the classifier, not on the classifier itself, and the relative performance of the selected feature sets would be roughly the same regardless of the classifier (with different absolute accuracy values).

This work introduces a unique dataset that enables, for the first time, single-pass interferometric coherence analysis with full polarimetric capabilities across multiple simultaneous frequencies. Such a configuration is not available in any current SAR satellite, making this study a novel contribution toward defining the technical requirements for future SAR missions that combine multiple data dimensions for advanced crop classification.

Building on this setup, the experimental design ensures a balanced contribution from all explored data dimensions: polarimetry, interferometry, multitemporal, and multifrequency. Since the multifrequency dimension includes only three bands, the remaining dimensions are similarly constrained to three or four features each. This prevents individual dimensions, such as polarimetry and time series, which independently achieve high classification performance, from dominating over others. A more exhaustive exploration of each individual dimension by adding more features lies beyond the scope of this study and is reserved for future work.

In summary, the novelty of this work lies in the comprehensive assessment of crop-type classification using combined polarimetric and interferometric features across multiple dates and frequencies. It demonstrates the complementarity between frequency bands driven by crop-specific responses at different growth stages and highlights the strong performance of PolInSAR features, both individually and in combination across temporal and spectral dimensions. Thus, this work is not aimed at improving the classification results over previous studies because there are no examples covering the same data dimensions. Instead, it is focused on understanding the role of all data dimensions considered in this combined framework.

II. Materials and Methods

A. Study Area and Reference Data

The study site, shown in Fig. 1, is located in the proximity of Wallerfing, Germany (48.70 N, 12.87 E). This is an agricultural area covering a relatively flat surface of about 4×6 km^2.

The reference data are composed of a geographical database that specifies the polygons, which define the agricultural fields and the corresponding crop types cultivated in each of them. The

Fig. 1. Map of the study area in Wallerfing (Germany) with all fields and crop types employed in the experiments.

TABLE II
Crop Types Present in the Study Area

Crop type	Number of fields	Total surface (ha)
Secluded arable land	22	16.60
Grasslands	9	8.05
Maize	54	111.03
Peas	2	8.73
Potatoes	11	37.82
Sugar beet	53	156.32
Vegetables	13	28.94
Winter barley	14	25.21
Winter rape	4	18.23
Winter wheat	93	195.30

reference dataset consists of ten crop classes. Table II provides the information of the number of fields and the total area for each crop type.

Winter wheat is clearly the most dominant crop type, followed by sugar beet and maize. In contrast, crop types, such as winter rape, grasslands, or peas, are the least represented. Overall, the study area comprises a variety of crop types with different distributions, which presents a suitable scenario for crop-type mapping applications.

Vegetation height and in-situ photographs of some fields of selected crop types are presented in Table III. The images show that the crop calendars of maize, winter wheat, winter barley, and winter rape are different. These four crop types were the only classes subject to dedicated in-situ measurements along the CROPEX14 campaign.

Regarding class denoted as "vegetables," it corresponds to a very general term, so the class may be quite heterogeneous and represent a variety of crops, such as carrots, cucumbers, etc. Unfortunately, there is no additional information about the precise plant species present in the fields included in the experiment.

All the fields assigned to "grassland" class are concentrated around a small part of the test site (see magenta fields in Fig. 1). However, this class denotes three different subclasses, i.e., grasslands including orchards, mowed pastures, and pastures. Consequently, this class is very heterogeneous, and we may

TABLE III
GROUND MEASURED HEIGHT AND PHOTOGRAPHS PRESENTING THE GROWTH STAGE OF MAIZE, WINTER WHEAT, WINTER BARLEY, AND WINTER RAPE CROPS AT THE DATES OF THE RADAR DATA ACQUISITIONS

	22 May	18 June	24 July
Maize	15 cm Leaf Development 	118–125 cm Stem elongation 	288–320 cm Development of fruit
Winter wheat	62–67 cm Stem elongation 	85–90 cm Development of fruit 	80–86 cm Ripening
Winter barley	90–92 cm Flowering 	80 cm Ripening 	Harvested
Winter rape	130–150 cm Development of fruit 	140–150 cm Ripening 	Harvested

expect bad classification results due to its spatial and temporal heterogeneity.

B. SAR Data and Preprocessing

The dataset employed in this study was obtained in the framework of the CROPEX14 campaign carried out in 2014 by the German Aerospace Center (DLR). The SAR data were acquired by the DLR's airborne F-SAR [32] system. This system has fully polarimetric and interferometric capabilities at different frequency bands, which make it unique to assess the joint exploitation of time series of PolSAR, InSAR, and PolInSAR features for crop classification. The dataset comprises images collected on 22 May, 18 June, and 24 July, for which SAR measurements at L-(1.3 GHz), C-(5.4 GHz), and X-(9.6 GHz) bands are available. The X-band and C-band acquisitions were carried out simultaneously, resulting in identical incidence angles and spatial resolutions, i.e., $0.5\,\text{m} \times 0.5\,\text{m}$ in azimuth and range directions. On the other hand, L-band data exhibit a coarser spatial resolution of $1.3\,\text{m} \times 0.5\,\text{m}$. Multiple spatial

baseline measurements were acquired. In this experiment, only one interferometric pair for each frequency band at each date is used. The three selected interferograms (at L-, C-, and X-bands) at each date present a similar height of ambiguity, around $3\,\text{m}$ at the scene center, for which different spatial baselines were chosen for each band.

From the available single-look complex (SLC) images gathered over the research area during the selected dates, a series of preprocessing steps are performed. They include the coregistration with respect to a reference image at each band and radiometric calibration.

In the construction of polarimetric and interferometric products, a spatial filtering is carried out with a boxcar filter of a kernel size of 23×23 at L-band, and 17×17 at C- and X-bands. With a pixel spacing of $0.19\,\text{m} \times 0.6\,\text{m}$ in azimuth and range directions in L-band, and 0.3m in both directions in C- and X-bands, the equivalent number of looks (ENL) is 94 in L-band and 104 in the latter ones. This corresponds to a final output resolution of 4.37 m × 13.8 m for L-band, and I5.1 m × 5.1 m

for the higher frequency bands, respectively. The final ENL and output resolution remain different from L- to C- and X-bands to avoid degrading the resolution of the higher frequency bands. Finally, a geocoding step is performed to transform the data to a geographic coordinate system. The input features exploited for classification are extracted from the geocoded data.

C. Definition of SAR Features

Starting from the SLC images provided by the SAR data for each polarimetric channel available, the following target scattering vectors at pixel level are formed:

$$\mathbf{k}_n = [S_{\mathrm{HH}}^n, S_{\mathrm{HV}}^n, S_{\mathrm{VV}}^n]^T \quad \forall n = 1, 2. \tag{1}$$

Superscript T denotes matrix transpose, and S_{PP}^n is the complex backscattering amplitude measured by transmitting and receiving vertical and horizontal polarizations, with $\mathrm{P} = (\mathrm{H}, \mathrm{V})$, at the nth end of the interferometric spatial baseline. The power of the complex backscattering amplitude is known as the backscattering coefficient, commonly denoted as σ_0 and expressed in logarithmic scale (dB).

To form interferograms, the scattering vectors $\mathbf{k}_n$ in (1) can be projected on a complex unitary vector $\mathbf{w}$, which indicates the selected polarization [29]. With that projection, each image of the interferometric pair is expressed as follows:

$$\mathrm{i}_n = \mathbf{w}^\dagger \cdot \mathbf{k}_n \tag{2}$$

in which the polarization is assumed to be the same in both images, i.e., $\mathbf{w}_1 = \mathbf{w}_2 = \mathbf{w}$, and the operator $\dagger$ represents the complex conjugate transpose. From (2), the PolInSAR coherence [29] is defined as the normalized complex cross-correlation between the two images i_n that form the interferometric pair at a selected polarization $\mathbf{w}$

$$\gamma(\mathbf{w}) = \frac{\mathbf{w}^\dagger \mathbf{\Omega}_{12} \mathbf{w}}{\sqrt{(\mathbf{w}^\dagger \mathbf{T}_{11} \mathbf{w})(\mathbf{w}^\dagger \mathbf{T}_{22} \mathbf{w})}}. \tag{3}$$

As a normalized magnitude, the PolInSAR coherence varies in $0 \leq |\gamma| \leq 1$. Considering fully polarimetric data, the matrix $\mathbf{\Omega}_{12}$ in the numerator is a 3×3 matrix, which contains the interferometric information, and the matrices $\mathbf{T}_{11}$ and $\mathbf{T}_{22}$ are 3×3 real positive semidefinite Hermitian matrices containing the polarimetric information of the primary and secondary images, respectively.

The variation of the PolInSAR coherence in (3) across the possible polarizations by means of $\mathbf{w}$ defines a region in the complex plane known as the coherence region (CoRe) [33], i.e., $\{\gamma(\mathbf{w}), \mathbf{w} \in \mathbb{C}^2, \|\mathbf{w}\| = 1\}$. The CoRe contains the complex coherences at the measured polarimetric channels, i.e., γ_{HH}, γ_{HV}, and γ_{VV}, as well as all the coherences for any projected polarization. In this sense, the coherences at the polarization states with maximum and minimum ground contribution, i.e., $\gamma(\mathbf{w}_{\max})$ and $\gamma(\mathbf{w}_{\min})$, are of particular interest due to their physical meaning. They correspond to the coherences located closest to the ground and to the canopy top, respectively. Another relevant coherence is the so-called trace coherence γ_{tr} [34], which represents the center of mass of the CoRe of the scene

(pixel) evaluated and is defined as follows:

$$\gamma_{\mathrm{tr}} = \frac{\mathrm{Trace}\,(\mathbf{\Omega}_{12})}{\sqrt{\mathrm{Trace}\,(\mathbf{T}_{11})\,\mathrm{Trace}\,(\mathbf{T}_{22})}}. \tag{4}$$

All these coherence measurements and derived parameters (e.g., the phase difference between them $\Delta\phi$), are evaluated as input features for classification.

D. Inspection of the Input SAR Data

With the purpose of inspecting the input dataset and understanding the complementarity between the different SAR data axes, polarimetric Pauli RGB composite images are presented in Fig. 2, and the Trace Coherence γ_{tr} is shown in Fig. 3.

Fig. 2 corroborates the polarimetric diversity of the data across time and frequency. Polarimetry [1] allows to distinguish between different types of scattering mechanisms, each associated with a specific physical interpretation. Thus, a dominant red color in a field (i.e., R=|HH-VV |) indicates a dominant dihedral type of scattering mechanism. Conversely, a dominant blue color (i.e., B=| HH+VV |) implies that surface scattering dominates the scene, while the green color (i.e., G=| HV+VH|) is mostly characteristic of dipoles and other type of scatterers typically observed in vegetation volumes.

According to the phenological stage of each crop and their structure, the different colors in the image show how different dominant scattering mechanisms vary with time and across frequencies. Longer wavelengths, e.g., L-band (24 cm) in the top row, penetrate into and through the vegetated canopy. In consequence, they allow to see a clearer dominant dihedral contribution located at ground level, which results from the interaction of the SAR signal with the ground and the stem of the plants. This translates into dominant red and pink colors, which evolve into greener ones as the season advances (second and third columns) and the plants grow. At the same time, such clear dihedral contributions are less pronounced as we move toward shorter wavelengths. This is observed at C-band (5 cm) in the middle row, and at X-band (3 cm) in the bottom row, for which the dihedral contribution is even less notable. The reason for this is that shorter wavelengths, such as X-band with its 3 cm, are not able to penetrate through dense canopies and are more sensitive to smaller scatterers. Hence, purple and blue colors, characteristic of surface type of scatterers, are more dominant over the majority of crops.

Analogously, Fig. 3 corroborates the interferometric diversity of the data across time and frequency. At L-band (first row), with its capability of penetration through the leaves and stems of the plants until the ground, an overall high coherence is observed at the evaluated dates for most crops. Only at the last day, 24 July, low coherence levels appear in specific fields. By looking at the crop-type, one can identify that most of these fields correspond to maize crops. By that date, they were fully developed with an average height of above 3m (see Table III), leading to the observed low coherence values. In contrast, C- and X-bands (middle and bottom rows) show overall lower coherence levels than L-band, being the lowest at X-band. This is a result of the sensitivity of these smaller wavelengths to small scatterers, such

Fig. 2. Pauli RGB composites corresponding to the three dates (Left: 22 May, Center: 18 June, Right: 24 July) and three frequency bands (Top: L-band, Center: C-band, and Bottom: X-band). The Pauli RGB channels correspond to R=|HH-VV|, G=| HV+VH |, and B=| HH+VV|.

as leaves and branches of the plants, which make the SAR signal to decorrelate faster. Only on the first date in May, most of the fields are in the early vegetative stages with very short or no plants, thus present high coherence levels.

Regarding the specific polarimetric and interferometric responses of each crop type, and their dependence on date and frequency band, they can be initially interpreted from Figs. 2 and 3 by observing the color-coded polygons. For maize (dark blue polygons), the fields are blue on 22 May, corresponding to the leaf development stage as reported in Table III, characterized by very short plants and a dominant surface scattering contribution. The maize fields are darker at L-band than at higher frequencies due to a weaker response from the soil rough surface at longer wavelengths. By 18 June, as the plants enter the stem elongation stage, an increased dihedral response is observed, causing the blue tone to fade. On 24 July, the L-band image exhibits a reddish tone over the maize fields, indicating strong dihedral interactions between the ground and stems. In contrast, X-band and C-band

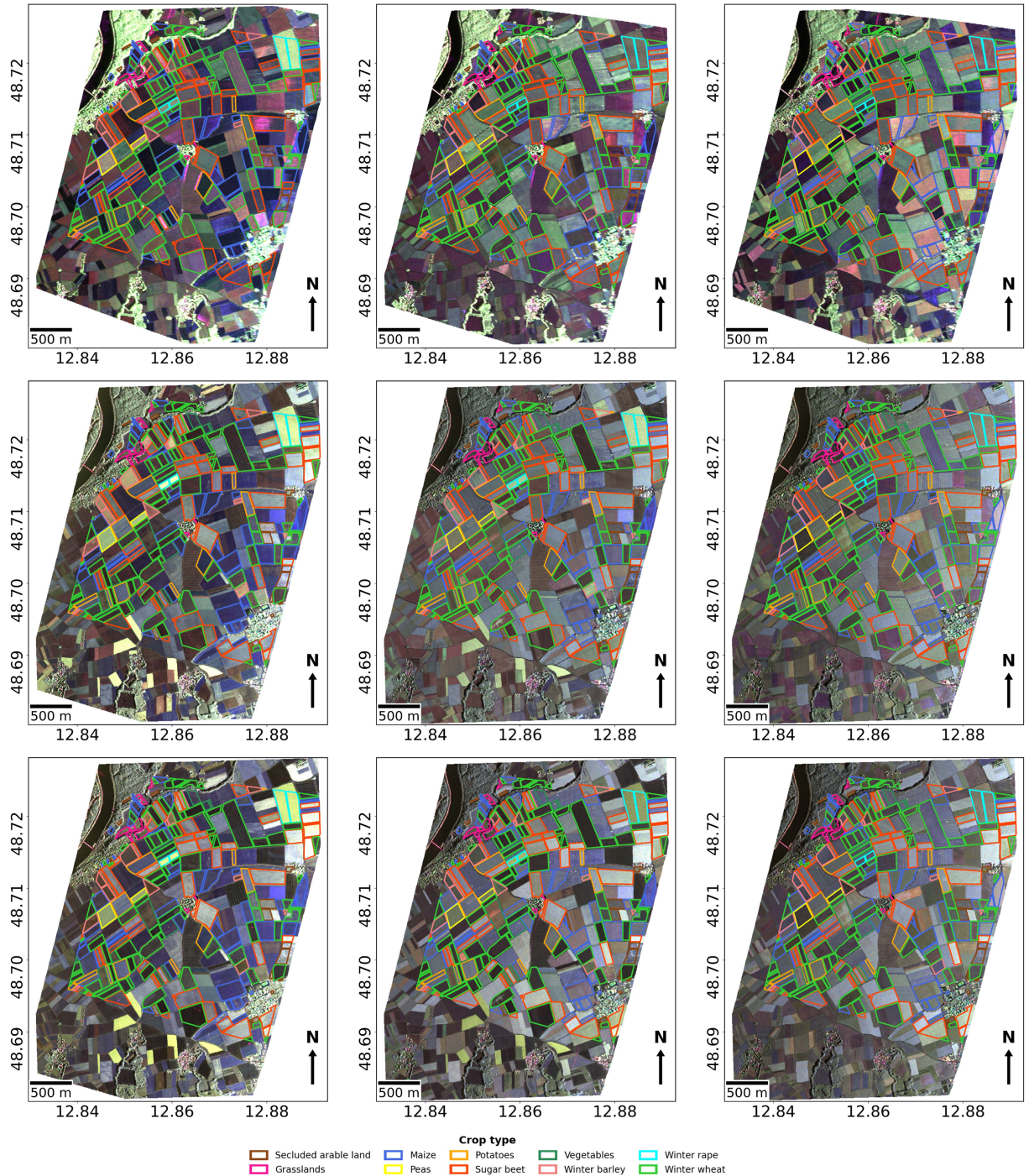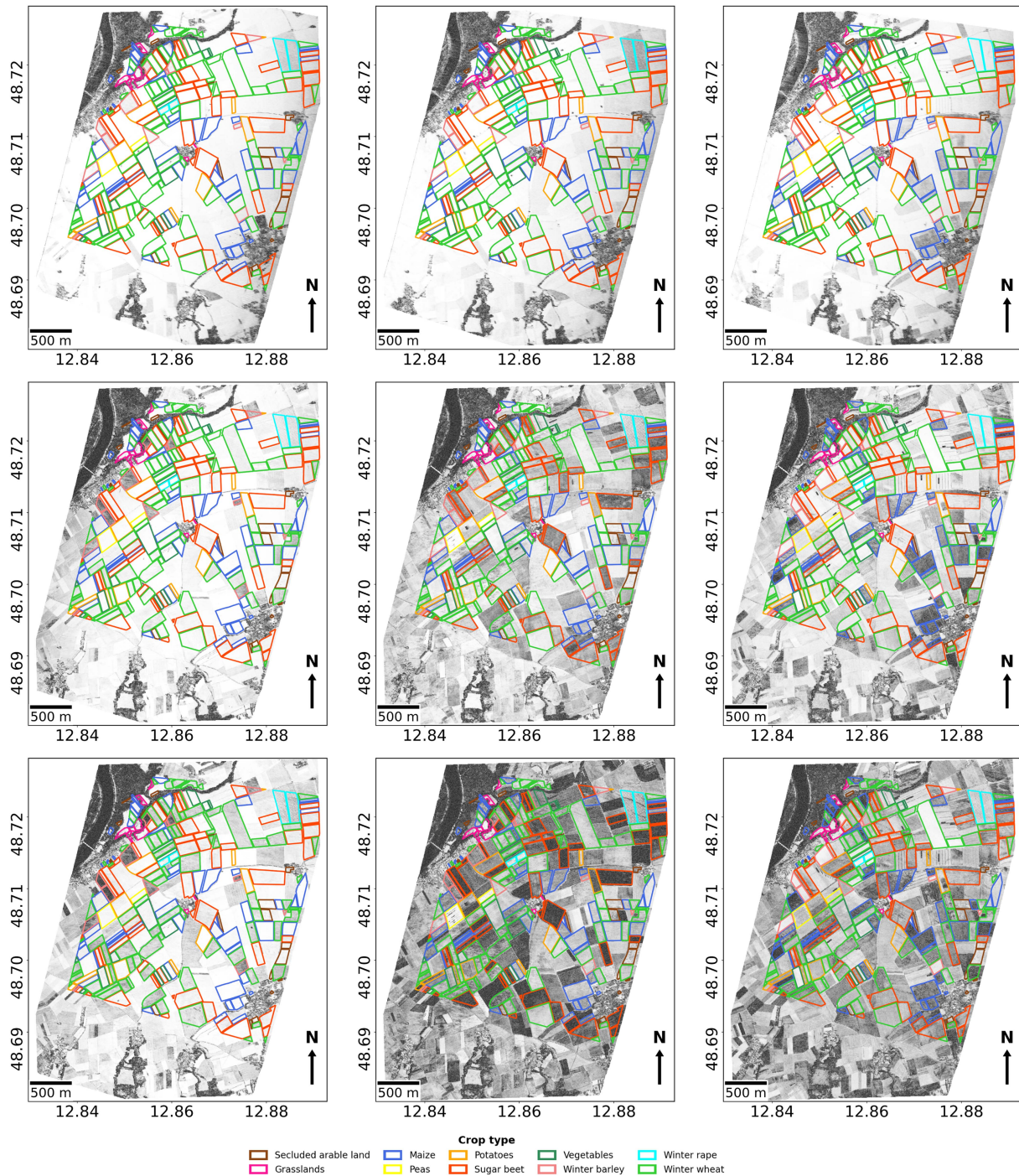Fig. 3. Trace coherence amplitude (0-black and 1-white) images corresponding to the three dates (Left: 22 May, Center: 18 June, Right: 24 July) and three frequency bands (Top: L-band, Center: C-band, and Bottom: X-band).

representations remain in gray color, similar to those from 18 June, due to their limited penetration capabilities. In Fig. 3, the coherence of the maize fields is very high (white in the images) at the first date for all bands, in accordance with the almost bare soil situation. Then, it decreases progressively across all bands as the crop height increases as a result of an increasing temporal decorrelation due to the increased amount of vegetation. At L-band, the coherence in the last date is higher than at the other two bands due to the stronger response from the ground, which is less affected by temporal decorrelation than the canopy.

Wheat (denoted with lime green polygons) presents a strong dihedral signature on 22 May at L-band, resulting in dominant purplish-red tones in the Pauli RGB representation (see Fig. 2). At 18 June, as stem elongation is completed during this period, an increased extinction makes the response to be lower, and hence the image is much darker. Notably, this effect is visible at all three bands. By 24 July, as the crop dries and enters the ripening phase, surface scattering becomes dominant, shifting the visual appearance towards blue. In Fig. 3, wheat shows relatively high coherence on 22 May due to its shorter canopy

and lower structural complexity. In particular, the coherence is very high at L-band, but the presence of the plants which are already in the elongation stage is evident at C-band and, more significantly, at X-band, for which, even if still high, the coherence is lower than at the larger wavelengths. As the crop height increases by 18 June, coherence decreases even more, especially at shorter wavelengths. As wheat transitions into the ripening stage, coherence gradually increases again, which indicates a reduction in volume scattering from the canopy and a stronger contribution from surface scattering. This results from dryer plants and bent stems at this later stage.

Winter barley (marked with pink-salmon polygons) exhibits a temporal evolution similar to wheat but matures earlier. It is harvested by 24 July, leading to pronounced surface scattering and consequently very high coherence values in the last date. Both wheat and barley show vertically structured canopies during early stages, resulting in observable dihedral and surface scattering responses depending on the phenological phase. Notably, in the RGB images of Fig. 2, the response at X-band is very similar at all three dates, whereas the L-band and C-band images show different values, hence being more sensitive to the changes in the crop associated with its development and its harvest.

Unlike these cereals, winter rape (cyan polygons) exhibits strong volume scattering (bright green color) on 22 May at all frequency bands, consistent with the fruit development stage. As the crop matures, volume scattering weakens, and after harvest, the fields appear bluish-purple due to the dominance of the surface component. The coherence trend for winter rape is similar across all three bands: initially decreasing due to canopy growth, and increasing again after harvest.

This diversity in the polarimetric and interferometric behavior of the SAR signal at different frequencies and throughout time for the different crop types establishes the basis of exactly what is exploited by the classifier.

E. Classification Strategy

1) Sets of SAR Features for Classification: This study is mainly focused on the performance of multifrequency PolInSAR data for crop classification. Therefore, to understand the contribution of the multifrequency data axis relative to all available data axes, different feature sets from each axis are evaluated both individually and in combination during the classification process. The analysis includes a detailed examination of the contribution of each frequency band and their performance in pairs and all together. Similarly, the impact of using individual acquisition dates versus all three dates simultaneously is evaluated. Finally, PolSAR and PolInSAR features are as well tested separately and in combination to determine their respective and joint contributions to the classification.

The input feature sets used are defined in Table IV. Four PolSAR features are employed: backscattering coefficient of HH, VH, and VV channels (in dB), and the normalized correlation between the copolar channels (HH and VV). Time series of such PolSAR features have already proven successful for crop classification applications, e.g., see [10] and [18]. In addition, the following four PolInSAR features are selected: absolute value

TABLE IV
POLARIMETRIC AND INTERFEROMETRIC SAR FEATURES FOR CLASSIFICATION

	Feature set	SAR observables
Set 1	**PolSAR**	$\sigma_{0_{HH}}$, $\sigma_{0_{VH}}$, $\sigma_{0_{VV}}$, $\rho_{HH,VV}$
Set 2	**PolInSAR 1**	γ_{tr}, $\gamma(\mathbf{w}_{max})$, $\gamma(\mathbf{w}_{min})$, $\Delta\phi_{max,min}$
Set 3	**PolSAR + PolInSAR 1**	Previous two sets together.
Set 4	**PolInSAR 2**	γ_{HH}, γ_{HV}, γ_{VV}, $\Delta\phi_{HH,VV}$

of the Trace Coherence [34], absolute value of the two extreme coherences with maximum and minimum ground contribution, and the height difference between the extreme coherences. As described in Section II-C, both the extreme phase coherence values and the trace coherence have shown a strong physical interpretation useful for the classifier to distinguish between crop types [30]. Finally, a third set of input features is as well tested to compare the contribution of individual interferometric coherences at different polarimetric channels (i.e., HH, HV, and VV) with respect to the previously described PolInSAR ones.

2) Classification Method. Single- Versus Multifrequency: The combination of different data sources in classification is usually carried out using the stacked-vector (SV) method [35], in which all individual features are used at once as input features of the classifier. Alternatively, fusion at the decision level using multiple classifiers can enhance results, as shown in Sentinel-1 and Sentinel-2 data fusion for crop-type mapping [36], [37]. This second approach is preferred in this work to establish a common framework for measuring the contribution of each data dimension. Nevertheless, one comparative example with the SV approach is as well included for completeness (see Section III-C).

For individual frequency bands, the RF algorithm [38] is employed, following the flowchart depicted in Fig. 4. RF provides explicit outputs (likelihood vectors) which enable the later use of the product of experts (PoE) [39] for the fusion of frequency bands (see description below).

The implementation employed in this work is provided by the scikit-learn package in Python [40] and was run mainly with default parameters. The number of trees was set to 500 to ensure a good performance and moderate computation time. The number of features considered when looking for the best split was left to the default value.

In order to prevent the classifier from having correlated pixels in both training and evaluation sets, we perform an initial field-level splitting: 50% of the fields for each class inside the reference data are assigned to the training dataset and the remaining ones to the testing dataset. Then, an extra step, called equitable random sampling in Fig. 4, is carried out to avoid the effect of the strong imbalance present in the number of pixels selected for each class inside the training dataset. It consists in choosing for every class the same number of pixels as the smallest class has. By doing so, all pixels of the smallest class are selected in the training dataset, whereas the pixels of the other classes are selected in the same amount but in a random way. After training the classifier, the prediction stage is carried out with all the pixels of the initial testing set. These are the pixels in 50% of the fields of each class resulting from the initial
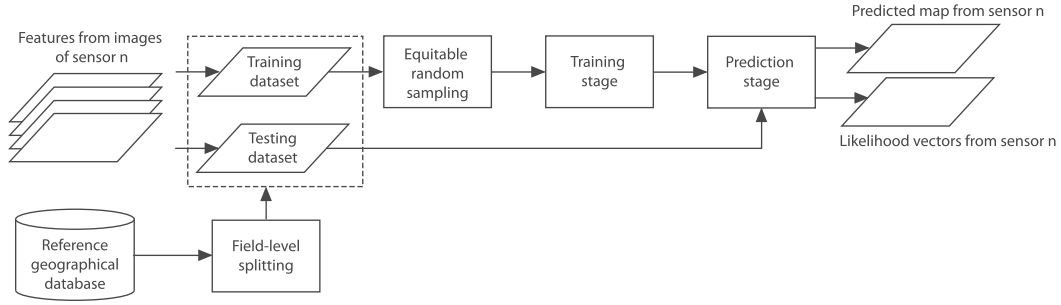
Fig. 4. Algorithm flowchart for the classification with individual frequency bands.

Fig. 5. Field boundaries of the training and testing fields for one of the ten realizations.

Fig. 6. Algorithm flowchart when merging the classification results coming from different frequency bands.

In the fusion methodology, illustrated in Fig. 6, probability vectors from individual band classifiers are combined using the PoE approach [39]

$$
P_{c_i}^{\text{Sens}_1, \text{Sens}_2, \dots \text{Sens}_N}(x) =
$$
$$
= \frac{P_{c_i}^{\text{Sens}_1}(x) P_{c_i}^{\text{Sens}_2}(x) \cdots P_{c_i}^{\text{Sens}_N}(x)}{\sum_{i=1}^{N} P_{c_i}^{\text{Sens}_1}(x) P_{c_i}^{\text{Sens}_2}(x) \cdots P_{c_i}^{\text{Sens}_N}(x)} \tag{5}
$$

where $P_{c_i}^{y}(x)$ stands for the likelihood of pixel x to belong to class c_i in classifier y for each of the corresponding sensors or available bands (i.e., L-, C-, or X-bands). The fused vector determines the final class for each pixel. Here, it is important to note that the same field-level splitting and equitable random sampling is applied to all bands to guarantee consistency across classifiers.

Finally, the RF algorithm is run ten times with different field splits. In each run, different training and testing datasets are employed in order to ensure unbiased accuracy metrics. The final accuracy metrics used to assess the classification performance are then computed from the confusion matrix resulting from the accumulation of the confusion matrices of the ten iterations.

The time required for running each one of the iterations of the classification (training, prediction, and evaluation) when all features are considered (frequency bands, dates, and feature sets) is 9 s in a conventional personal computer with 32 GB RAM. This is very short because the study area is small in extent. Therefore, computational cost is not a relevant issue in this work.

It is important to clarify that, despite the field-level splitting and the equitable random sampling, some residual spatial correlation may be present in the data used for classification. However, this would impact all experiments to the same degree and,

field-level splitting. For illustration purposes, Fig. 5 presents the fields selected for training and testing in one of the runs of the classification, resulting from the 50% field-level splitting.

As displayed in Fig. 4, the output of the algorithm consists in a probability vector, for each testing pixel, indicating its likelihood to pertain to any possible class. For the classification with an individual frequency band, the highest probability found in each vector defines the final predicted class chosen for each pixel. For the classification with combinations of bands, the likelihood vectors are exploited as described next.

consequently, it does not affect the comparison of classification results obtained using different sets of radar features, which is the main purpose of this manuscript.

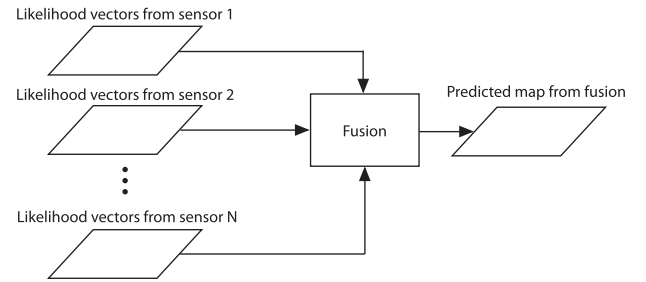*3) Evaluation of Classification Results:* The metrics selected for the evaluation of the classification results include the overall accuracy (OA), producer's accuracy (PA), user's accuracy (UA), and F1-score. They are computed from the confusion matrices from the reference set [41], and they are known to provide detailed insights into the contribution of each input dataset to specific classes.

OA indicates the global performance of the classifier, i.e., how well the classifier performed across all classes, whereas the other three metrics (PA, UA, and F1-score) are computed for each class. For a given class, PA is the probability that a pixel that is truly in that class was correctly labeled by the classifier. Therefore, PA is focused on errors of omission, since a low PA means the classifier missed a lot of the actual class, i.e., it underpredicted the class. As for UA, it is the probability that a pixel labeled as a class on the resulting map is actually of that class on the ground. UA is focused on errors of commission because a low UA means there are many false positives, i.e., the classifier overpredicted the class. Consequently, PA and UA are complementary, and, for each class, they assess the classifier detection power and the reliability of the result for a user, respectively. Finally, the F1-score is the harmonic mean of PA and UA, and hence, it provides a single score that balances the tradeoff between these two metrics. In this sense, the F1-score is useful for comparing the performance on different classes.

III. RESULTS

A. Classification Results and Performance Analysis

1) Overall performance: First, as a general measure of the overall classification performance for all crop types, the OA is presented in Table V.

The first block of this table shows the results obtained using only polarimetric features (*PolSAR* set). When a single-frequency band at a single date is used, i.e., as in a conventional fully polarimetric SAR acquisition, the best band depends on the date. This demonstrates the importance of the wavelength in polarimetry. The polarimetric signature of the elements in a vegetated scene depends strongly on the vegetation element size and the wavelength, as well on the microwave penetration depth. The different growth status of the crop types present in this test site at the three observation dates makes the three bands to perform differently at different dates.

Regarding the combination of two bands, the pair formed by L- and X-bands is generally the best, which can be explained by the largest difference of their wavelengths, and hence their greatest complementarity as sources of physical information. Using two bands at a single date improves always more than 10% the OA with respect to one band alone, which is quite remarkable. Finally, the combination of the three bands outperforms by 2%–4% all band pairs when single dates are exploited.

The analysis of the results obtained by PolInSAR features alone (*PolInSAR 1* and *PolInSAR 2* sets) evidences that this data

TABLE V
OA FOR ALL THE EVALUATED CASES

Features	Bands	OA (%)			
		22 May	18 June	24 July	All 3
PolSAR	L	58.61	65.72	61.89	88.46
	C	69.01	58.37	50.36	87.83
	X	64.60	73.48	51.34	89.60
	L, C	80.57	78.58	70.69	93.12
	L, X	79.05	84.10	73.36	94.15
	C, X	75.50	78.01	62.03	91.87
	L, C, X	82.81	85.88	75.29	94.30
PolInSAR 1	L	37.49	47.34	43.17	77.05
	C	44.78	31.26	45.82	72.92
	X	41.81	32.48	32.10	73.66
	L, C	56.38	58.15	56.27	87.54
	L, X	60.16	58.63	50.47	88.58
	C, X	54.98	40.22	49.14	79.50
	L, C, X	64.23	62.36	58.37	88.98
PolSAR + PolInSAR 1	L	72.37	77.54	75.91	90.85
	C	75.96	69.98	68.24	90.46
	X	76.76	80.13	71.47	92.47
	L, C	83.06	86.09	79.84	94.63
	L, X	83.92	89.30	82.60	95.73
	C, X	80.80	85.36	76.36	93.62
	L, C, X	84.79	90.07	82.58	95.64
PolInSAR 2	L	34.74	50.29	42.74	77.58
	C	50.06	39.55	46.87	76.23
	X	45.00	35.79	33.65	74.45
	L, C	59.53	64.70	57.04	88.17
	L, X	59.93	62.67	51.49	88.72
	C, X	59.57	48.28	50.17	81.23
	L, C, X	66.96	68.50	59.23	89.53

dimension is much worse for crop classification than polarimetry, providing OA values between 5% and 40% worse than the *PolSAR* set. Using a single band at a single date, L- and C-bands are better than X-band.

Notably, as it happened with polarimetry alone, combining the PolInSAR features of two bands at one date improves more than 10% the OA with respect of single bands, and the three bands together further improve by 2%–4% the OA provided by band pairs.

Although PolInSAR performs worse than PolSAR, it is sensitive to different properties of the crops, and therefore, their combination clearly improves the OA provided by PolSAR alone in all cases, i.e., for one band, for pairs of bands, and for the three bands together. In fact, the worst OA at a single band and one date is just below 70%, and the results provided by the *PolSAR* and *PolInSAR 1* sets are the best ones in the table.

The complementarity of polarimetry and interferometry makes also the performance of pairs of bands to improve clearly. The joint use of L- and X-bands at single dates provides OA values very close to the OA achieved with all three bands, hence showing again the relevance of combining long and short wavelengths to maximize the information content in the data. For instance, OA levels of around 90% are obtained on 18 June, when most of the crops, even if at different phenological stages, have plants almost or fully developed with an already defined structure.

The combination of polarimetry and interferometry could be evaluated also by combining the *PolSAR* set with the *PolInSAR*

TABLE VI
PA FOR ALL THE EVALUATED DATES

Features	Bands	PA (%)									
		Arable land	Grasslands	Maize	Peas	Potatoes	Sugar beet	Vegetables	Winter barley	Winter rape	Winter wheat
PolSAR	L	66.52	91.41	96.11	95.78	68.79	89.98	82.74	51.17	98.93	92.65
	C	68.86	84.95	88.48	96.37	57.84	85.20	87.57	81.56	99.29	95.45
	X	74.60	72.30	87.49	97.85	62.21	92.14	93.07	79.99	99.71	94.30
	L, C	73.10	94.24	96.85	97.86	67.43	94.29	93.49	79.66	99.67	97.26
	L, X	76.32	90.05	96.92	98.17	73.19	96.29	94.62	83.63	99.78	96.85
	C, X	73.88	83.10	90.68	98.47	66.43	92.57	94.96	89.02	99.72	96.83
	L, C, X	74.97	90.70	96.49	98.36	71.09	95.51	96.40	90.72	99.76	97.53
PolInSAR 1	L	38.96	69.06	89.47	66.61	62.26	67.26	86.41	70.94	96.14	80.96
	C	63.09	57.22	85.36	78.58	35.33	79.46	46.94	84.73	86.70	69.10
	X	59.48	61.77	80.06	87.39	39.77	80.78	51.20	75.90	87.84	73.05
	L, C	60.05	74.61	92.31	90.91	60.60	87.72	80.79	86.17	98.63	90.98
	L, X	59.21	82.30	92.27	96.15	66.57	88.76	82.61	81.57	98.88	92.25
	C, X	65.28	68.22	87.32	86.30	44.37	85.56	54.30	84.07	93.90	79.02
	L, C, X	64.55	80.33	92.49	93.45	61.56	90.60	77.62	87.75	98.97	92.38
PolSAR + PolInSAR 1	L	62.98	91.52	97.59	97.99	63.89	91.85	88.38	68.39	99.63	94.94
	C	77.09	93.18	92.57	98.85	52.55	89.45	90.21	97.12	99.76	95.43
	X	83.35	86.78	91.38	98.68	65.05	96.14	94.05	85.67	99.86	95.30
	L, C	76.90	96.81	97.25	98.98	68.12	94.91	96.79	95.74	99.89	97.97
	L, X	83.63	95.84	97.39	98.94	72.75	97.71	97.41	92.52	99.93	98.00
	C, X	83.00	92.27	93.11	98.84	66.25	95.30	95.88	96.00	99.89	96.80
	L, C, X	83.16	96.12	96.94	98.95	72.58	96.87	97.54	97.21	99.92	98.15
PolInSAR 2	L	44.61	81.90	89.16	73.18	54.72	68.61	74.95	73.56	97.19	84.24
	C	61.48	64.14	84.77	88.04	56.88	81.63	54.27	84.32	87.71	74.20
	X	57.38	66.25	79.84	90.89	48.87	82.13	56.75	81.73	85.32	72.86
	L, C	65.07	84.67	92.02	94.99	66.31	87.64	81.78	92.93	98.85	92.02
	L, X	66.87	89.34	91.39	97.80	65.09	88.25	81.66	89.54	98.95	93.50
	C, X	67.09	71.95	86.49	92.46	61.69	86.38	61.01	85.45	93.08	81.27
	L, C, X	71.97	87.00	91.75	96.48	69.34	89.93	83.43	94.21	98.94	92.71

2 set instead of the *PolInSAR 1* set, and the results would be equivalent. In this case, the *PolInSAR 1* set is selected because it is formed by features derived from the geometry of the loci of the PolInSAR data on the complex plane, and they provide representative physical information of the scene (pixel) evaluated (see Section II-C). Instead of just using features (coherences and phase differences) derived from the data expressed in the linear basis as with the *PolInSAR 2* set, the PolInSAR 1 set departs from a direct application of interferometry in the linear channels. Still, the results of the combination with PolSAR data do not depend on the PolInSAR set selected.

Results show that, for any of the input feature sets employed for the classification, high levels of accuracy are always obtained when exploiting time series of multifrequency data. In particular, the highest OA levels are obtained when all three dates (last column) and, at least, two frequency bands, are used in the classification. Again, for most of the feature sets, employing the two frequency bands with the shortest and longest wavelength possible (i.e., X- and L-bands) provides results as accurate as when using the three wavelengths available.

2) Performance for Different Classes: To further provide insights into specific crop classes the PA, UA, and the F1-score metrics obtained when the three dates are used are presented in Tables VI–VIII, respectively.

Evaluating the PA results in Table VI for all crops globally, one can observe clear differences between crop types which are mostly correctly identified by the model, and others for which many true instances are missed, resulting in a high number of false negatives. Those which are best classified are winter rape and peas, followed by maize and winter wheat. In all cases, the highest PA scores (above 99% in the case of the winter rape) are obtained when exploiting both polarimetric and interferometric features for classification, as well as more than one frequency band.

Using PolSAR and PolInSAR information at a single frequency band, crops like winter rape and peas achieve PA values close to 99% as they did when using the same combination of features but with more than one band. Instead, using only PolSAR features the PA achieves similar values (around 99%) independently from how many bands are used for winter rape, whereas there is a slightly improvement with two or three bands for peas with respect to a single band.

However, multifrequency information helps avoiding false negatives when the specific crop type is not that perfectly identified by the model. This is the case of crops, such as winter wheat, maize, or even sugar beet. There are as well other crops for which the difference of introducing multifrequency data in order to be correctly identified is even more pronounced. For instance, vegetables achieve a maximum PA score of 98% when using multifrequency PolSAR and PolInSAR data. Nevertheless, they barely reach 94% if only one frequency band is used.

On the other hand, examples of crops for which many instances are missed by the model, even when exploiting multispectral input features, are arable land or potatoes. These

TABLE VII
UA FOR ALL THE EVALUATED DATES

Features	Bands	Arable land	Grasslands	Maize	Peas	Potatoes	Sugar beet	Vegetables	Winter barley	Winter rape	Winter wheat
		UA (%)									
PolSAR	L	50.24	48.61	96.59	73.57	64.09	92.60	81.00	67.79	92.78	95.94
	C	48.86	43.22	93.26	81.70	56.22	91.47	63.50	96.57	93.97	98.76
	X	52.17	29.12	92.53	96.54	62.50	96.34	73.97	90.87	98.92	98.89
	L, C	64.47	50.19	97.16	82.83	87.16	94.11	75.56	95.44	95.12	99.45
	L, X	65.69	42.97	96.33	95.23	90.16	96.72	84.53	94.51	99.63	99.23
	C, X	58.28	39.79	94.08	94.07	69.18	96.21	74.44	99.07	99.73	99.39
	L, C, X	65.14	45.57	96.42	97.17	90.20	96.58	79.51	97.22	99.80	99.59
PolInSAR 1	L	12.51	28.65	93.32	41.90	55.69	80.53	88.34	79.14	94.25	91.82
	C	41.45	14.32	88.92	56.09	35.52	86.93	35.90	89.62	42.44	91.05
	X	35.67	21.99	84.80	64.47	29.68	89.95	46.97	76.92	42.35	93.11
	L, C	34.57	36.53	96.67	95.19	58.03	91.26	82.85	96.77	89.72	96.76
	L, X	35.55	40.50	96.30	94.81	60.65	93.32	85.51	95.29	91.75	96.91
	C, X	50.19	25.53	90.96	68.20	43.61	89.55	48.96	90.11	47.39	95.66
	L, C, X	45.51	39.94	96.65	95.20	58.15	92.35	79.69	97.13	86.68	97.88
PolSAR + PolInSAR 1	L	50.08	53.94	97.74	96.79	74.09	93.30	74.39	90.79	98.35	95.38
	C	60.76	56.92	97.24	97.66	61.85	92.60	60.23	98.45	97.95	98.48
	X	71.36	40.02	94.19	96.75	70.37	97.03	75.34	97.26	99.30	99.41
	L, C	67.25	59.90	99.05	98.55	91.00	95.20	72.09	98.52	98.12	99.34
	L, X	77.71	54.67	98.00	98.23	92.64	97.22	78.84	98.58	99.39	99.42
	C, X	71.33	53.25	97.81	97.95	76.73	95.92	69.53	99.08	99.44	99.44
	L, C, X	74.45	57.66	98.91	98.33	93.40	96.73	75.14	98.87	99.59	99.66
PolInSAR 2	L	17.50	35.90	94.64	34.81	50.13	80.97	70.58	83.79	95.06	94.40
	C	36.48	15.36	94.43	58.85	42.68	89.47	62.92	90.50	44.80	95.47
	X	32.28	23.27	90.44	49.74	32.32	91.10	64.35	81.23	37.18	95.16
	L, C	38.69	39.18	97.51	94.21	61.72	90.99	80.75	98.62	91.61	98.33
	L, X	41.65	43.33	97.45	94.13	59.51	91.38	84.34	97.77	92.33	98.08
	C, X	46.68	25.85	95.71	63.37	46.74	92.04	70.67	91.35	48.37	97.46
	L, C, X	50.27	41.72	97.95	96.93	62.39	92.68	85.01	98.05	88.62	98.64

TABLE VIII
F1-SCORE FOR ALL THE EVALUATED DATES

| Features	Bands	Arable land	Grasslands	Maize	Peas	Potatoes	Sugar beet	Vegetables	Winter barley	Winter rape	Winter wheat
		F1-score (%)									
PolSAR	L	55.95	62.96	96.34	82.12	64.40	91.15	81.08	57.04	95.74	94.26
	C	55.32	57.07	90.79	87.09	54.60	88.02	72.89	88.06	96.48	97.07
	X	60.78	40.66	89.91	97.18	60.03	94.10	81.85	84.59	99.31	96.52
	L, C	66.93	65.12	97.00	88.85	74.30	94.11	83.06	86.48	97.27	98.34
	L, X	69.36	57.30	96.61	96.63	79.46	96.45	88.87	88.53	99.71	98.02
	C, X	64.25	53.19	92.33	96.06	65.59	94.26	82.97	93.56	99.72	98.08
	L, C, X	68.39	60.08	96.44	97.75	77.92	95.97	86.72	93.78	99.78	98.54
PolInSAR 1	L	18.56	39.28	91.28	50.81	57.00	72.78	87.13	73.92	95.11	85.94
	C	48.93	22.33	86.94	63.10	32.81	82.83	38.99	86.61	56.28	78.45
	X	43.31	31.38	82.27	71.72	31.90	84.95	46.57	74.56	55.72	81.64
	L, C	42.45	47.89	94.34	92.95	57.51	89.23	81.42	91.01	93.83	93.75
	L, X	42.82	53.39	94.17	95.40	61.66	90.75	83.91	87.70	95.13	94.50
	C, X	55.08	36.31	88.95	74.21	41.00	87.33	49.41	85.97	61.54	86.40
	L, C, X	51.47	52.20	94.44	94.26	57.57	91.27	78.17	91.88	92.31	95.03
PolSAR + PolInSAR 1	L	54.34	67.51	97.66	97.35	67.37	92.41	79.87	77.66	98.97	95.12
	C	66.56	70.36	94.74	98.25	52.59	90.83	71.72	97.77	98.84	96.89
	X	76.50	53.20	92.67	97.70	64.44	96.53	83.14	90.45	99.58	97.29
	L, C	71.06	73.74	98.13	98.76	76.35	94.96	81.87	97.09	98.99	98.65
	L, X	80.31	69.13	97.69	98.58	79.89	97.42	86.46	95.32	99.66	98.70
	C, X	76.17	67.04	95.29	98.39	67.45	95.53	80.11	97.43	99.66	98.09
	L, C, X	78.15	71.76	97.91	98.64	80.17	96.75	84.14	98.03	99.75	98.90
PolInSAR 2	L	24.54	48.94	91.69	46.60	51.48	73.97	70.86	76.86	96.11	88.99
	C	44.82	24.02	89.28	68.52	46.75	85.05	57.23	86.81	58.31	83.36
	X	40.82	33.61	84.75	61.68	37.82	86.00	59.45	80.93	51.10	82.43
	L, C	47.28	52.18	94.61	94.52	62.57	89.14	80.69	95.67	95.06	95.06
	L, X	50.69	57.19	94.26	95.82	60.61	89.60	82.60	93.43	95.52	95.73
	C, X	53.98	36.77	90.82	73.39	50.99	88.77	64.74	87.77	62.24	88.46
	L, C, X	58.17	54.39	94.68	96.65	63.76	91.07	83.96	96.06	93.43	95.54
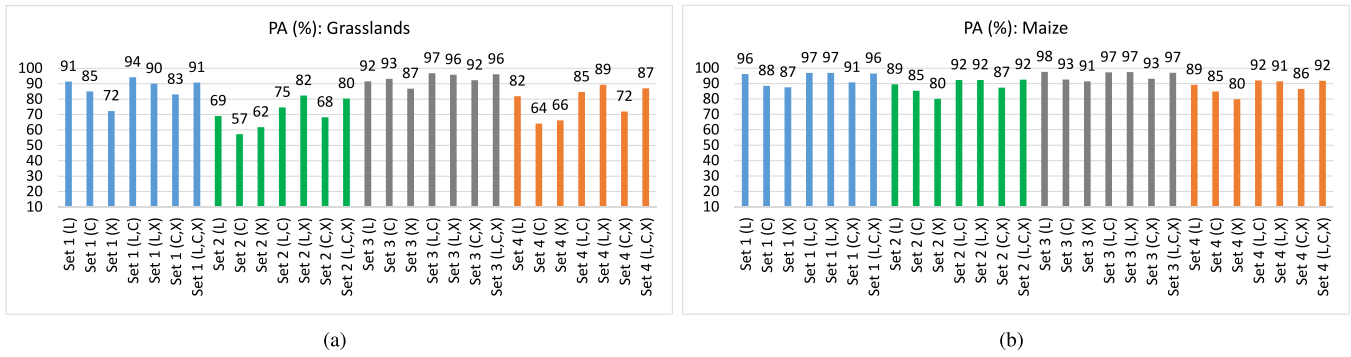
Fig. 7. Bar plots representing the PA scores at pixel level for the crop types (a) grasslands and (b) maize considering different input feature sets. For simplicity, *Set 1* refers to *PolSAR* features, *Set 2* to *PolInSAR 1*, *Set 3* to PolSAR + PolInSAR 1, and *Set 4* to *PolInSAR 2*, respectively.

crops are poorly detected by the model when exploiting single PolInSAR datasets for inversion, with PA scores of around 65%. Even if they improve when including PolSAR and PolInSAR features together, the sensitivity of the model to them is still not optimum, reaching a maximum PA of 84% for arable land and 73% for potatoes, respectively. This is somehow an expected behavior for such classes, given that arable land has no plants and those of the potato crops are very short (less than one metre) at any point of their growing cycle.

In general, the PolInSAR datasets alone at a single frequency do not provide a sufficient level of sensitivity of the model to any crop type. In addition, although most crops are better detected when using multifrequency PolInSAR data than with single-frequency PolInSAR, higher PA values are generally obtained when exploiting PolSAR data than using only PolInSAR data.

An interesting case is that of the winter barley, which is the one most benefited from incorporating PolInSAR features as input for classification. While using polarimetric features alone the PA reached is 91%, this crop is much better detected, with an accuracy of up to 97%, when adding PolInSAR information. As observed in Table III, this can be explained by the fact that during the observation period, the barley crop transitions from an early vegetative stage, i.e., dense plants around 1 m with high water content, to a late reproductive one with fully dried plants around 80 cm and even bent and flat. In addition, it is already harvested when observed at the last date available, i.e., 24 July. This entails a strong coherence change that goes from low to high values at the end of the season. Hence, making them suitable features for classification.

A more detailed analysis of the PA score is provided in Fig. 7 for two specific classes that are characterized by a different plant morphology, i.e., grasslands and maize. They present a very different physical structure and are also representative of other crops, so they serve to illustrate how the plant structure plays a key role in detecting and identifying different crop classes accurately.

Grasslands are a seminatural type of vegetation class characterized by very short (in the order of centimeters) and elongated soft green leaves, which remain with a similar structure throughout the observation period. In consequence, features sensitive to height (and its changes), as those including interferometric

information (i.e., *PolInSAR 1* and *PolInSAR 2* datasets) do not provide the model with the sensitivity required to properly distinguish them. PA levels remain below 90% even when using multifrequency data. In this case, polarimetric features sensitive to the dominant type of scattering mechanism present, yield better PA results. Values of 90% accuracy are reached even with L-band alone, in which a clear surface component is expected to be dominant for this crop at such a low frequency.

Maize plants, on the other hand, are observed throughout their whole growing cycle. From the early vegetative stages in 22 May with small and distanced plants of around 15 cm, to the late reproductive ones in 24 July with dense plants that overpass the 3m (as seen in Table III). The observation of such changes in height makes the PolInSAR features more suitable for the identification of this crop type than in the case of grasslands. PA levels of almost 90% are already reached at L-band using either the *PolInSAR 1* or *PolInSAR 2* datasets. Using polarimetric observables alone, also yields high PA levels. Those obtained at L-band are even in the order of the ones reached when using multifrequency data. Such levels, above 96%, are not possible to obtain with single frequency C- or X-band data. The explanation for this lies on the dominant vertical orientation of the stalks of the maize plants, which appears as a dominant dihedral contribution at ground level at L-band.

The reliability of the RF model to precisely classify each crop type is summarized in the UA results presented in Table VII. Different to the PA results, which showed the winter rape as the best identified crop by the model, the UA results indicate that winter wheat is the most accurately predicted crop, with the least number of false positives. Crops, such as winter rape, winter barley, and maize, follow in confidence levels. All of them reach UA values above 99% when using PolSAR and PolInSAR features at different frequency bands simultaneously for classification. Similar accuracy values are also retrieved when employing the individual polarimetric or interferometric feature sets and multiple frequencies, with values over 97% for maize and around 99% for winter barley, among others. For both crop types, the UA levels decrease considerably (up to a 10% decrease) in the absence of multifrequency data.

A case worth highlighting is the winter rape crop. Very high UA levels are obtained when using polarimetric data alone (i.e.,
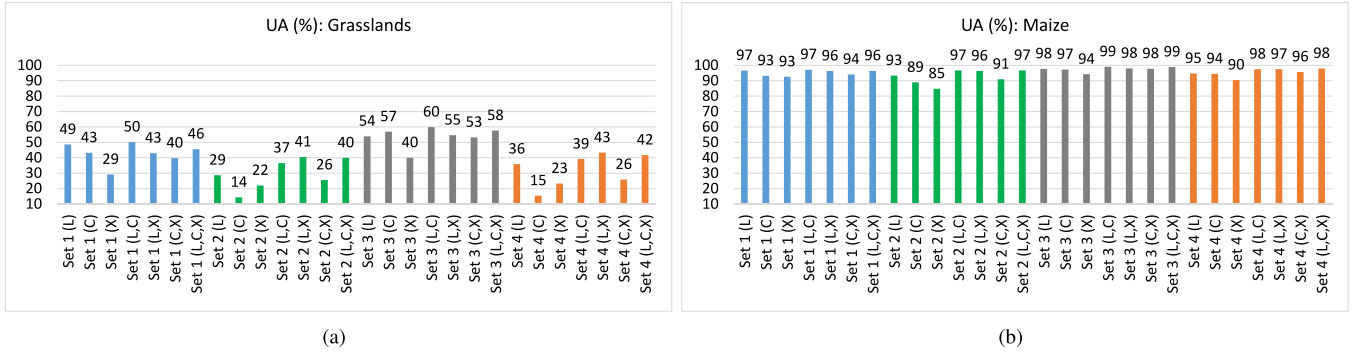
Fig. 8.   Bar plots representing the UA scores at pixel level for the crop types (a) grasslands and (b) maize considering different input feature sets. For simplicity, *Set 1* refers to *PolSAR* features, *Set 2* to *PolInSAR 1*, *Set 3* to PolSAR + PolInSAR 1, and *Set 4* to *PolInSAR 2*, respectively.

>99%), yet very low ones are reached when using only the interferometric coherences, as seen with either the *PolInSAR 1* or *2* datasets. For this specific crop, it is important to highlight the strong dependence of the accuracy on the frequency. While UA levels above 90% are observed whenever L-band data are employed, the accuracy reached with higher frequency bands, i.e., C- and X-bands, remains below 50%. Within the observation period, from May to July, this crop is fully developed with plants above 1 m. This is as well observed in Table III. The characteristic randomness in the structure of the rape plants yields similar coherence levels, which are likely to be low, especially at higher frequency bands for fully developed plants.

On the other side, arable land, grasslands, vegetables, and even potatoes cannot be taken as reliable estimates of the model. Regardless of the use of both polarimetric and interferometric information, together with multispectral data, maximum UA values below 80% are obtained for arable land and grasslands. In the case of the vegetables, even if the instances of this crop seem to be accurately retrieved according to the PA values, a number of false positive decreases the reliability of its classification, with UA values also below 80%. UA values slightly above 90% are reached for the potato crops only when all input features at the different bands available are used. Such relatively low accuracy values for these crops can be explained by the similarity in their plant structure, for instance, between potatoes and vegetables, or even between arable land and grasslands, hence yielding a lower precision in the classification with a considerable number of false positives.

Similarly to the analysis performed over the PA score, Fig. 8 displays a detailed focus on the UA performance on grasslands and maize crops. While the PA results showed that grasslands can be properly identified, especially when using PolSAR data and low frequencies as input for classification, the UA results manifest a different situation. Their constant structure of short thin leaves observed across the growing season leads to the inability of the model to produce reliable grassland estimates, amounting to a large number of false positives.

Maize crops exhibit the opposite behavior. The confidence of their correct classification remains high with UA levels consistently above 90% even when using only single-frequency data for almost all individual datasets evaluated. It increases to above 95% whenever making use of multifrequency information. The advantage of the multifrequency information is particularly evident when exploiting PolInSAR data. Since the full growing of this crop is observed, from a couple of centimeters up to 3 m tall plants, the interferometric coherence evolves from very high values to low decorrelated ones. In addition, this sensitivity of the interferometric coherence to changes in the phase center height according to the growing of the maize plants is strongly frequency dependent. A dominant dihedral contribution coming from the interaction of the SAR signal between the ground and the stalks is visible at L-band, but not at C-band or X-band. For these last bands, the scattering phase center is located at higher parts of the plants, where the signal decorrelates when interacting with the leaves, fruits, and remaining scatterers that are not transparent enough to short wavelengths.

To finish the analysis of the RF model performance on crop classification, the F1-score results are presented in Table VIII. In a single metric, the F1-score summarizes the reliability and accuracy of the classification by equally weighting both types of errors: false negatives (i.e., PA) and false positives (i.e., UA).

Examples of crop types that are consistently correctly classified are wheat and maize. Classification results are optimum regardless of the input feature set used, including those without exploiting multifrequency data. Both are relatively well detected through high PA values, and confidently estimated with even higher UA percentages. This results in maximum F1-scores that overpass the 98% accuracy, with minimum values that oscillate around 80% when exploiting single-frequency data alone. As observed in Table III, these crops have in common that the observation period encompasses different phenological stages. The already grown wheat plants undergo a drying out period, with heights from around 1 m to 80 cm. While for the maize, we observe the full growth from almost bare soil up to 3m tall plants.

Peas and winter rape are also examples of crops that are properly classified, reaching overall F1-scores of 98% and even above 99%, respectively. However, differently to the commented wheat and maize crops, peas, and winter rape are characterized by relatively short plants in which the individual scatterers within the canopy are randomly oriented. In consequence, the performance when exploiting single-frequency PolInSAR data for classification is reduced. Accuracy levels below 70% are
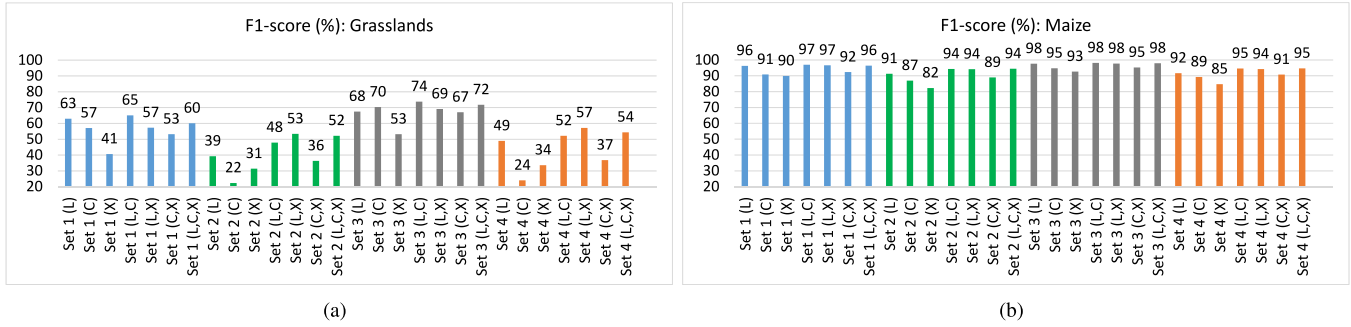
(a)

(b)

Fig. 9. Bar plots representing the F1-score at pixel level for the crop types (a) grasslands and (b) maize considering different input feature sets. For simplicity, *Set 1* refers to *PolSAR* features, *Set 2* to *PolInSAR 1*, *Set 3* to *PolSAR + PolInSAR 1*, and *Set 4* to *PolInSAR 2*, respectively.

retrieved in these cases, with the exception of L-band data for winter rape classification.

Another set of crops that are, even if not so accurately, also fairly well classified, are sugar beet and winter barley. The contribution of multifrequency data proves to be key in achieving here high classification scores. Accuracy levels of around 80% when using single-frequency PolInSAR data increase in more than 10% when exploiting multifrequency information. F1-scores up to 91% are reached for sugar beet, and even up to 96% for winter barley.

The performance of the classification for the remaining crop types is not optimum. On the one hand, potatoes and the crops classified as arable land present consistent low classification accuracy. F1-score values oscillate, in the best case, around 80% for both crops. In the case of arable land, the lack of plants suppresses the information content of the input feature sets evaluated. A similar situation arises for the potatoes, characterized by plants of a couple of tens of centimeters.

At last, crops, such as vegetables and grasslands, even though they are correctly detected, the reliability of their classification is rather poor. Thus, their low rate of false negatives (i.e., PA of 95% for multifrequency PolInSAR data) comes at the expense of a high rate of false positives (i.e., UA below 80% for vegetables, and lower than 60% for grasslands). The result is final F1-score levels below 90% for vegetables and under 75% for grasslands, respectively.

The final classification results for grasslands, as well as for maize crops, can be corroborated in detail in the graphs shown in Fig. 9. As advanced by the UA levels, contrasting classification accuracy is retrieved for each of these two crops. The low level of confidence when classifying grasslands yields F1-score levels below 80% for any feature set evaluated. This diverges from that of the maize, which maintains scores higher than 80% even in the worst cases, and up to 98% in the best ones with the use of multifrequency data.

B. Classification Map

A visual evaluation of the classification results following the PoE fusion methodology together with an RF classifier is presented in Fig. 10. It includes the predicted map and the assessment (i.e., correct versus incorrect) map. The result shown in this figure corresponds to the joint use of PolSAR and PolInSAR
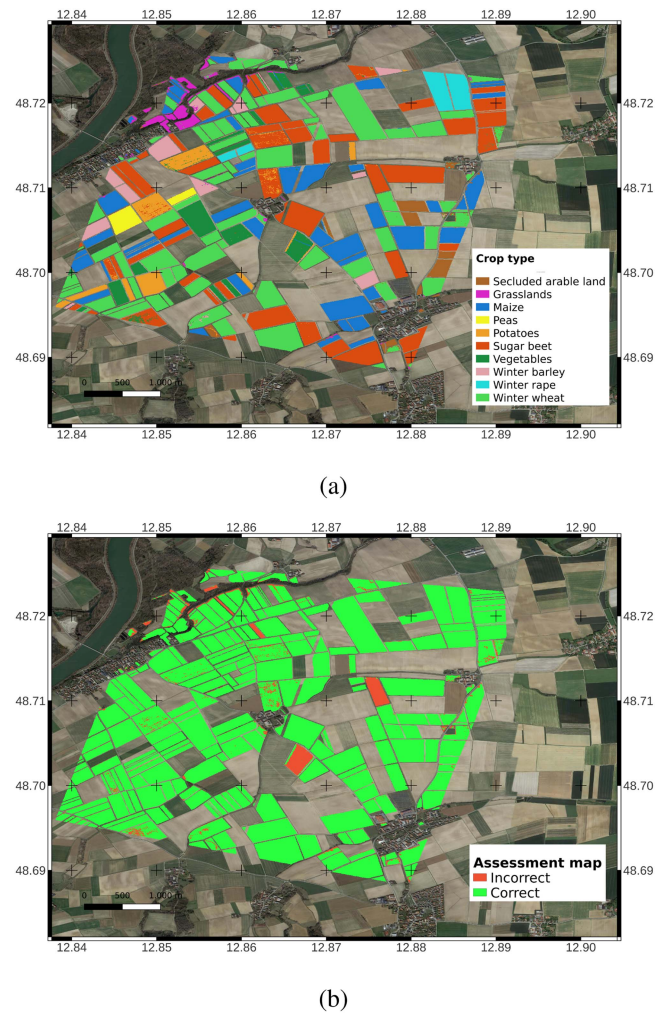

(a)

(b)

Fig. 10. Map of the classification result obtained by using the Set 3 of features at all frequency bands and dates. (a) Classification map (predicted classes). (b) Assessment map.

features at all three bands and all three dates. Instead of showing the classification maps of each one of the ten realizations, which are predicted over only half of the fields (due to the 50% field split carried out explained in Section II-E2), here we have computed a global map in which the class assigned to each pixel corresponds to the class that has been most assigned in the set of all ten

realizations. Since the OA reached with this set of features is higher than 95%, the predicted map [shown in Fig. 10(a)] is visually very similar to the reference crop-type map (see Fig. 1).

From the inspection of the associated assessment map [shown in Fig. 10(b)], one can identify three types of errors. In first place, there are some fields with a proportion of erroneous pixels randomly distributed over them. For instance, there is a big sugar beet field in the center of the image in which some pixels are wrongly classified as potatoes, and contrarily in another field located to the left. This type of error is present wherever the two classes share similar radar features and the images exhibit fine spatial resolution. In many practical applications, if field boundaries are known and each field is cultivated with a single crop type, an additional processing step can be implemented. This step involves assigning the most frequent class to the whole field, thus minimizing the impact of these errors.

The second type of error corresponds to edge effects either due to fences (covered or formed by plants, i.e., bushes) or produced by small geo-referencing errors. In such situations, pixels located in the edge of a field may be misclassified. In our experiment, this happens in the top left part of the test site for a group of fields of wheat, maize, and sugar beet that are adjacent to a curved line of trees (along a small river or a path). The edge of these fields is wrongly classified as grasslands. Similar to the previous error type, if the classification product is to be provided at field scale rather than at pixel scale, it could be solved by assigning the most frequent class (i.e., the mode) within the field as the class of the whole field.

The third type of error happens when a whole field, or almost its entirety, is classified as another class. In our experiment, this happens for two big fields of potatoes in the center of the scene, which are classified as vegetables and sugar beet, respectively, and for a narrow field of sugar beet in the top left part, which is classified as vegetables. In the assessment map they appear as polygons fully colored in red. The most plausible cause of this type of classification error is a mislabeling, i.e., fields for which the class indicated in the reference data set is wrong. Unfortunately, such a situation is very common and inherently reduces the achievable accuracy. Some strategies have been recently developed to tackle the impact of mislabeled crop fields in crop type classification [42], [43].

C. Comparison With the SV Approach

With the purpose of completing the analysis of the classification performance provided by the combination of polarimetric, interferometric, multitemporal, and multifrequency data, this section presents the results of the crop classification following an SV approach [35]. To this end, analogous metrics to those presented in the previous sections, including OA, PA, UA, and F1-score are computed and presented in Tables IX–XII, respectively. In this case, for the sake of brevity the results are constrained to the case in which all available frequency bands (i.e., L-, C-, and X-bands) are exploited jointly as input.

The accuracy results given by the OA, i.e., Table V for the PoE approach and Table IX for the SV methodology, indicate very similar performances. Even if slightly higher OA levels

TABLE IX
OA FROM THE SV APPROACH FOR ALL THE EVALUATED DATES

Features	Bands	OA (%)			
		22 May	18 June	24 July	All 3
PolSAR		85.44	88.85	80.60	94.44
PolInSAR 1	L, C, X	64.79	66.63	60.63	87.32
PolSAR + PolInSAR		85.85	91.52	83.47	95.28
PolInSAR 2		65.83	71.29	60.99	87.75

are observed in the PoE when exploiting multitemporal data (last column), the difference with respect to those in the SV is minimum.

In general, when the different data sources (i.e., different frequency bands) provide complementary information, a fusion performed at feature level, as in the SV approach, is expected to provide optimum results. This is confirmed in this case, since the OA values obtained are very similar to those obtained in the case of the PoE methodology.

Regarding the rest of metrics (PA, UA, and F1-score), the same trends as those commented in Section III-A following the PoE method are observed with a classification based on the SV approach. This corroborates the consistent contribution of the different feature sets to classify the crops present in the study site.

Focusing on crop-level performance, crops whose observation period spans distinct phases of their growth calendar, which entail clear structural and water content changes, are consistently identified and classified with high accuracy. This is the case of winter wheat, winter rape, winter barley, maize, or peas. Following either the PoE or the SV approaches, F1-scores of around 98% and higher are reached when exploiting multifrequency PolInSAR information.

Conversely, classes representing seminatural scenarios rather than crop types exhibit poor classification performance across all evaluated methods. For instance, arable land achieves F1-scores below 80%, while grasslands fall below 75%. Moreover, the presence of these classes increases confusion among short crop types with a not very defined structure. Examples of this are potatoes and vegetables, which achieve F1-scores in the order of 80% and 85%, respectively, using both methods.

With respect to the performance of the evaluated approaches at feature level, the results from the PoE and SV methods exhibit strong consistency. When the entire observation period of the crop calendar is observed, the sensitivity of the scattering phase center to plant height variations makes PolInSAR data, particularly the interferometric coherence, a suitable feature for classification. In contrast, classes with relatively homogeneous structures from a radar perspective over time benefit significantly from the joint use of both polarimetric and interferometric parameters for classification. Hence, for both methods, the highest classification scores are obtained when the datasets *PolSAR* and *PolInSAR 1* are employed as input features.

Overall, the comparable accuracy and optimal classification results retrieved from either the PoE or the SV fusion methods can be attributed to the proposed methodology. As described in Section II-E2, the initial dataset undergoes two key steps prior to the classification: an initial split at field-level and an

TABLE X
PA FROM THE SV APPROACH FOR ALL THE EVALUATED DATES

Features	Bands	PA (%)									
		Arable land	Grasslands	Maize	Peas	Potatoes	Sugar beet	Vegetables	Winter barley	Winter rape	Winter wheat
PolSAR	L, C, X	75.99	95.91	96.08	97.90	70.04	96.19	96.37	95.56	99.83	97.31
PolInSAR 1		66.04	73.10	92.52	97.43	70.52	86.96	84.94	92.53	98.10	88.86
PolSAR + PolInSAR 1		81.59	95.39	97.48	98.91	71.16	96.97	96.97	97.64	99.91	97.45
PolInSAR 2		68.06	84.66	92.20	98.10	69.08	88.14	82.07	93.57	98.13	89.40

TABLE XI
UA FROM THE SV APPROACH FOR ALL THE EVALUATED DATES

Features	Bands	UA (%)									
		Arable land	Grasslands	Maize	Peas	Potatoes	Sugar beet	Vegetables	Winter barley	Winter rape	Winter wheat
PolSAR	L, C, X	66.89	52.96	97.22	97.26	93.27	95.60	80.73	96.77	99.88	99.84
PolInSAR 1		39.92	32.45	95.94	94.80	62.92	91.95	82.89	95.00	94.49	97.91
PolSAR + PolInSAR 1		76.39	61.76	98.70	99.37	91.96	95.53	81.27	97.97	99.75	99.50
PolInSAR 2		44.02	32.35	96.24	93.97	62.81	91.98	82.68	96.73	95.66	98.63

TABLE XII
F1-SCORE FROM THE SV APPROACH FOR ALL THE EVALUATED DATES

Features	Bands	F1-score (%)									
		Arable land	Grasslands	Maize	Peas	Potatoes	Sugar beet	Vegetables	Winter barley	Winter rape	Winter wheat
PolSAR	L, C, X	70.23	67.53	96.63	97.53	79.05	95.88	87.26	96.05	99.86	98.55
PolInSAR 1		48.80	42.07	94.09	96.02	64.88	89.21	83.20	93.69	96.03	93.03
PolSAR + PolInSAR 1		77.63	74.48	98.08	99.14	79.69	96.22	87.67	97.78	99.83	98.46
PolInSAR 2		52.43	44.10	94.09	95.83	64.39	89.85	81.85	95.06	96.87	93.65

equitable random sampling. This second step ensures that the same number of pixels of each class is used in the training. Thus avoiding a possible overfitting of predominant crop classes. Without it, an unbalanced number of training data potentially leads to overfitting when the fusion is performed in the early stages.

D. Analysis of Feature Importance

The importance of all the features employed in the classification is analyzed in this section by considering the feature importance provided by the RF classifier. For this purpose, we focus on the experiment with the SV approach in which the whole set of features was employed, i.e., three dates, three frequency bands, and PolSAR + PolInSAR data.

The importance of each one of the 72 features, averaged over ten iterations, is shown in Fig. 11. The features with highest contribution correspond to the VH backscattering coefficient measured on 22 May at C-band (4.5%), at X-band (4.3%), and at L-band (3.4%), followed also by the VH backscattering coefficient measured on 24 July at L-band (3.3%), on 18 June at C-band (2.9%), and on 18 June at X-band (2.9%). Then, the following most important features correspond to the trace coherence measured at L-band on 18 June (2.5%) and 24 July (2.5%). These eight features come from different frequency bands and dates, and include both backscatter (at VH channel) and interferometry (trace coherence), demonstrating the contribution of all data dimensions considered in this study. Moreover, the eight features together only provide 26% of importance,

hence proving also the value of the rest of features to improve the classification performance.

The analysis of feature importance can be carried also by grouping the importance values as a function of the feature magnitude type, their acquisition date, and their frequency band. Regarding their magnitude type, Fig. 12 presents the importance of the eight different radar features considered. As previously mentioned, the backscattering coefficient of the cross-polar channel (VH) contributes the most to the classification (25.46%), followed by the HH backscattering coefficient (15.57%) and the trace coherence (14.54%). At the other extreme, the copolar correlation contributes the least (6.13%).

In the same vein, the importances of the features can be grouped based on whether they belong to the *PolInSAR 1* or *PolSAR* dataset (see Table IV). Fig. 13 shows that the PolSAR features, accounting for 59%, are more helpful to the classifier than those from the PolInSAR features, which account for 41%. However, the difference is not so high, which reveals that the interferometric features also provide valuable information for classification.

Following the same logic, we can group the features by date, regardless of their nature (see Fig. 14). This graph shows that features acquired on 22 May contribute the most (40%) to distinguishing among classes, but the importance of the other two dates is around 30% each, which is not much smaller than the first date.

Finally, we can also group the features based on the frequency used (L-, C-, or X-band). The result, shown in Fig. 15, clearly
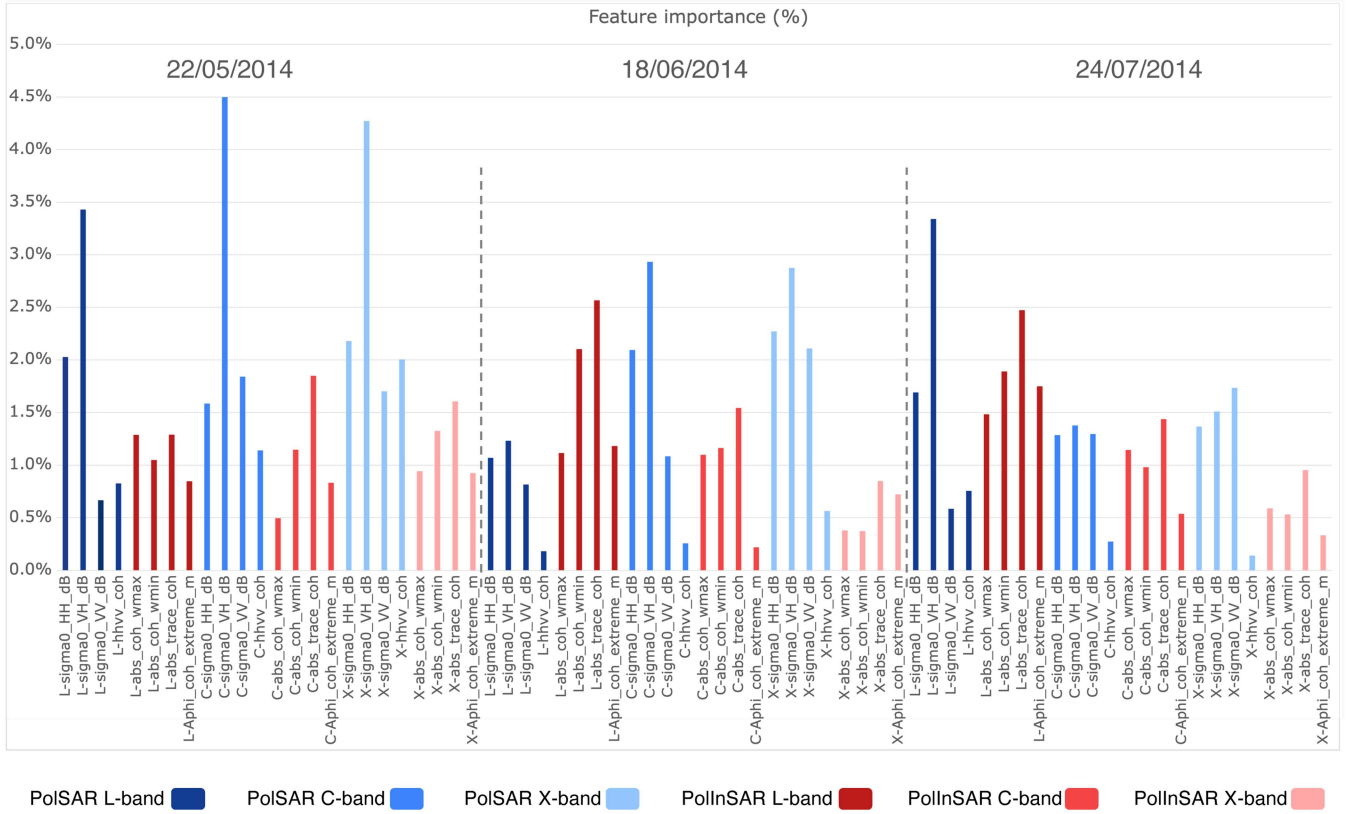
Fig. 11.   Importance for all individual SAR features used in the SV approach with three dates, three frequency bands, and PolSAR + PolInSAR data.
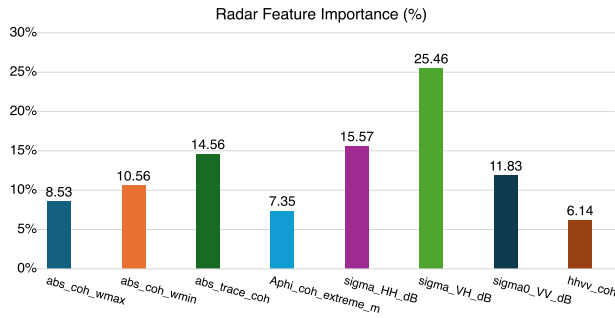

Fig. 12.   Importance for the eight individual SAR features grouped by their magnitude type.
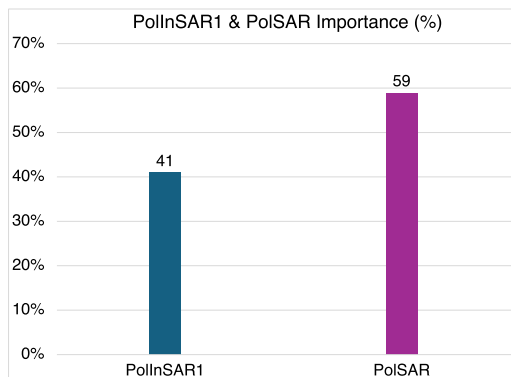

Fig. 13.   Importance of the features grouped into PolInSAR and PolSAR.
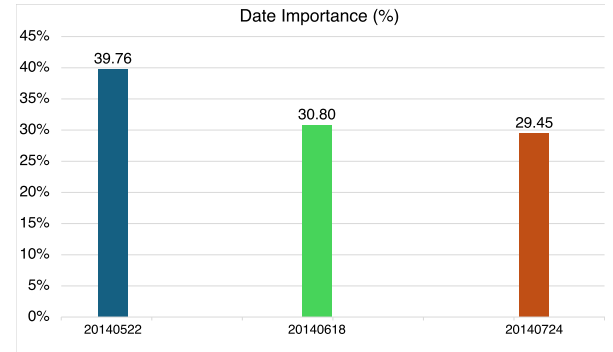

Fig. 14.   Importance of features depending on the date.

demonstrates that all three bands contribute in a balanced way to the classification performance. Although L-band appears to be predominant (35.65%), its importance is very similar to the other two bands, i.e., 32.10% and 32.24% at C- and X-bands, respectively.

IV. DISCUSSION

The classification results previously exposed are discussed here in comparison to observations from related works. There are different aspects to consider attending to the data axes evaluated: time series, polarimetry, interferometry, and multifrequency. Special emphasis is placed on integrating all of them with
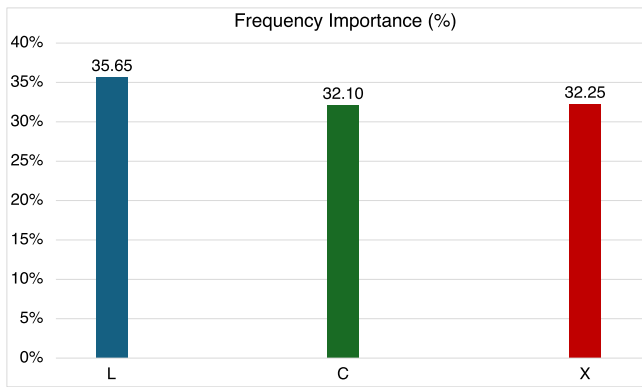
Fig. 15.   Importance of features depending on the frequency band.

multifrequency. In this sense, the literature is mostly limited to their separated results, rather than to their effective combination.

The relevance of time series for crop classification is clear. Time series is related to the crop calendar, and the crop calendar defines the main temporal pattern of the structure and water content of the plants. The fact that a dense time series yields better accuracy results had already been proven in several works, e.g., [9], [10], [16], and [28]. However, the findings in this article highlight that, rather than a dense time series, what is even more critical is that the selected dates cover different crop growing stages. This was also found in [44]. Regardless of the density of a time series, if only a part of the growing cycle in which the plants do not undergo important structural and water changes is covered, it will not provide the most optimum results.

In this regard, the current dataset is limited to three months of observation, from which only three dates have been analyzed. With it, we find proof of the relationship between having specific dates of different growing phases versus amount of dates. At the dates evaluated, i.e., 22 May, 18 June, and 24 July, the maize crops go from an average height of $15\,\mathrm{cm}$, to 1 m and over 3 m, respectively. Such a change, from almost bare soil to a very large biomass content with 3 m plants, is key for the high classification accuracy reached with this crop.

The lack of observation of such changes results in a poor performance for certain classes. For instance, those which are not really cultivated crops but rather semi-natural vegetation, e.g., arable land and grasslands. This goes in line with the findings of other experiments, as those presented in [37]. F1-scores of around 62% for grasslands and 41% for fallow were obtained in [37] with dual-pol Sentinel-1 C-band data. In the same order of accuracy, 57% and 55% F1-score are obtained for the equivalent grasslands and arable land classes exploiting only polarimetric observables at C-band in our results. Masking out these seminatural classes would potentially improve the final OA. Nevertheless, we have maintained them with the purpose of designing a methodology as general as possible, without the need of prior knowledge of which crops are kept fallow, or from which ones we expect to obtain agricultural products.

Another evidence of the impact of the temporal pattern of plant structure and water content is found in the winter wheat and winter barley crops. The very similar structure of these two cereals makes them prone to be confused. This was observed in [45], as well as in [16], for which a large error for the winter barley crop was highlighted when using cross-polarization backscatter. However, despite their resembling plant structure, the confusion level between them in the present experiment is not strong. UA levels (cf., Table VII) over 97% for winter barley and 98% for winter wheat are obtained when exploiting full-pol interferometric data at either C- or X-bands alone, and around 99% when exploiting several bands together. The reason for this is their different crop calendar. As shown in Table III, the crop development of winter barley is faster than that of winter wheat.

In both [10] and [31], among the frequency bands evaluated (L- and C-bands in the first case, and L-, C- and X-bands in the second case), C-band seemed to be preferred one for crop classification. The results obtained here differ from this observation, since L-band provides better results than C-band in many cases. The longer wavelength at L-band allows it to penetrate into and through the vegetation, and this impacts the sensitivity of this band to the whole plant. Hence, L-band is able to interact with the plant from top to bottom, and is not just limited to the upper layers, as are C-band and, in greater measure, X-band. Such a better performance of L-band is clearer when exploiting PolInSAR features in crops like winter rape, maize, and winter wheat. A crop that seems to perform worse at L-band than at higher bands is winter barley. This could be explained by the frequent confusion between barley and winter wheat, as they are two crops with very similar structure and physical features [16]. Shorter crops, such as peas and sugar beet, are better classified at X-band than at other lower bands because the X-band wavelength is enough to penetrate the whole volume and, at the same time, provide a response not so affected by the soil.

Regarding the use of multifrequency data, the results found in this work go in accordance to those in [10] and [31]. In all cases, the joint exploitation of multiple frequencies improves the OA with respect to a single band. For instance, an improvement of up to 13% in [10] was observed when exploiting C- and L-band data together. However, there are additional observations that can be extracted from this work. It is correct that the best results are consistently obtained with multifrequency data over single-frequency. Nonetheless, results here suggest that the use of two frequencies (L- and X-bands) with wavelengths that are the furthest away from each other provide already the same level of accuracy as when including a third band (C-band) with similar wavelength to one of them.

It is worth noting that the acquisition of SAR data at different frequencies (i.e., with different sensors and/or configurations) entails normally that the resulting spatial resolution in the images at each band is different. In our case, this happens at L-band, which has a different resolution with respect to C- and X-bands (see Section II-B). A resolution difference is expected to impact the generation of high-resolution final products with a pixel size similar to the resolution of the SLC images. Each pixel on ground may correspond to one image pixel at some bands and more pixels at other bands. However, in our experiment, the data were spatially filtered in the estimation of the PolSAR and PolInSAR variables to ensure a high ENL. They present a much degraded

resolution with respect to the original images and, as a result, no impact on the classification results coming from this difference in spatial resolution is expected.

V. CONCLUSION

The performance of crop classification based on multispectral radar data formed by multitemporal polarimetric and interferometric features has been evaluated. This work is unique in providing, for the first time, an evaluation of the multifrequency contribution to crop classification isolated from other factors, such as polarimetric channels, incidence angle, spatial resolution, and acquisition dates. These factors are primarily determined by the sensor and acquisition geometry. Notably, fully polarimetric and interferometric data acquired with the same sensor (F-SAR) at the same dates within the context of the CROPEX14 campaign were exploited. Therefore, the only parameter that changes notably across the data is the frequency band, i.e., with data available at L-, C-, and X-bands. Such an evaluation covering all SAR data axes has never been done before.

The first overall conclusion is that all the dimensions of the data contribute to improving classification performance when they are jointly exploited. For instance, using only PolSAR data from one band at one date, the OA ranges between 50% and 73%. When a second band is added, the OA ranges between 62% and 84%, and with all three bands, it is between 75% and 86%, depending on the date. Similarly, using PolSAR features at a single band but including the three dates, the OA is between 87% and 90%. This further improves with two bands (91% – 94%) and three bands (94.3%). Similarly, jointly using PolSAR and PolInSAR features at a single band and one date improves between 7% and 20% the OA of PolSAR alone.

The main improvements provided by the different data dimensions are summarized next, together with the characteristics that make them relevant.

1) *Multitemporal:* Crops are well separated if dates cover different phenological stages of the crops along their growing season and also out of that time frame. A few dates could suffice if the calendar of the crops present are different enough.
2) Polarimetry contributes when the morphology of the crops present is diverse, for which sensing at different dates clearly helps.
3) Interferometry seems to perform as the worst information source, but its contribution is unique. This is demonstrated by the improvement of performance when it is used in conjunction with polarimetry and/or time series.
4) Multifrequency improves classification in all cases as a result of the strongly different response of crops at different frequency bands. In fact, the best results from pairs of frequency bands are provided by the most extreme wavelengths (L- and X-bands).

The experimental setup of this work is quite unique because it comes from a dedicated airborne campaign. Therefore, the transfer of our conclusions to satellite data gathered by operational sensors presents some limitations.

Single-pass interferometry (or repeat-pass with very short temporal baseline) is limited to satellite constellations formed by two or more satellites with coincident orbital configurations. Currently, this is only the case for TanDEM-X. Moreover, the spatial baseline required for offering sensitivity to crops (i.e., short vegetation) is much longer than for other applications (e.g., forestry).

Polarimetry is usually restricted to dual-pol systems (e.g., Sentinel-1), with only a few sensor offering quad-pol data (e.g., Radarsat-2 at C-band and ALOS-2 PALSAR-2 at L-band). In addition, quad-pol acquisitions are not routinely gathered, favoring the dual-pol mode because of its larger spatial coverage (swath). In this context, compact-pol (as provided by the Radarsat Constellation Mission) offers enhanced polarimetric information with respect to dual-pol.

Regarding the use of multifrequency data, to date we need to rely on different satellite sensors, normally operated independently by different agencies. This situation may improve with the launch of ROSE-L (an L-band radar part of the Sentinel expansion missions), which is foreseen to operate in a coordinated way with Sentinel-1.

In the meantime, there are other L-band satellites (either launched or that will be launched in the next future) that should be tested for crop monitoring (e.g., SAOCOM, ALOS-3 PALSAR-4, and NISAR) in combination with X-band sensors (e.g., TerraSAR-X, TanDEM-X, PAZ, COSMO Sky-Med, etc.).

The experimental setup presented in this study was deliberately designed to ensure a balanced assessment of all evaluated data dimensions (polarimetry, interferometry, multitemporal, and multifrequency). To this end, each dimension was constrained to three or four representative features, reflecting the most restrictive case. This controlled configuration allowed meaningful comparisons without biasing the classifier toward any single dimension, while still delivering strong classification performance. Future work may extend this analysis by incorporating a broader set of features, including additional polarimetric descriptors (e.g., decomposition-based features), more acquisitions dates to form time series, and further interferometric variables, such as diverse spatial baselines and features derived from the complex CoRe.

Due to the required data acquisition scheme, so far only possible with airborne systems, the study was carried out over a small agricultural region. However, under comparable SAR system capabilities, our conclusions could be directly transferred to different landscapes and larger regions. In such cases, variations in classification performance are primarily driven by weather and climate conditions. Accordingly, certain features may present different values due to factors, such as plant water content, with fluctuations between rainy and dry seasons, or soil moisture differences resulting from varying irrigation practices, among others. Even so, how these variations reflect in the input features would be used by the classifier to discern between crop types, and the classification and fusion strategy for the different frequency bands would remain unchanged. With regard to larger regions, they would require data gathered by satellites, but the size of the evaluated region is not expected to severely affect the overall classification performance.

Acknowledgment

References

[1] J.-S. Lee and E. Pottier, *Polarimetric Radar Imaging: From Basics to Applications*. Boca Raton, USA: CRC Press, 2009.

[2] J.-S. Lee, M. Grunes, and E. Pottier, "Quantitative comparison of classification capability: Fully polarimetric versus dual and single-polarization SAR," *IEEE Trans. Geosci. Remote Sens.*, vol. 39, no. 11, pp. 2343–2351, Nov. 2001.

[3] T. Ainsworth, J. Kelly, and J.-S. Lee, "Classification comparisons between dual-pol, compact polarimetric and quad-pol SAR imagery," *ISPRS J. Photogrammetry Remote Sens.*, vol. 64, no. 5, pp. 464–471, 2009.

[4] S. Hariharan, D. Mandal, S. Tirodkar, V. Kumar, and A. Bhattacharya, "Multi-frequency polarimetric SAR data analysis for crop type classification using random forest," in *Synthetic Aperture Radar (SAR) Data Applications*. Heidelberg, Germany: Springer Nature, 2023, pp. 195–217.

[5] V. Turkar, R. Deo, Y. S. Rao, S. Mohan, and A. Das, "Classification accuracy of multi-frequency and multi-polarization SAR images for various land covers," *IEEE J. Sel. Topics Appl. Earth Observ. Remote Sens.*, vol. 5, no. 3, pp. 936–941, Jun. 2012.

[6] B. Guindon, P. Teillet, D. Goodenough, J. Palimaka, and A. Sieber, "Evaluation of the crop classification performance of X, L and C-band SAR imagery," *Can. J. Remote Sens.*, vol. 10, no. 1, pp. 4–16, 1984.

[7] K. Chen, W. Huang, D. Tsay, and F. Amar, "Classification of multifrequency polarimetric SAR imagery using a dynamic learning neural network," *IEEE Trans. Geosci. Remote Sens.*, vol. 34, no. 3, pp. 814–820, May 1996.

[8] D. Hoekman and M. Vissers, "A new polarimetric classification approach evaluated for agricultural crops," *IEEE Trans. Geosci. Remote Sens.*, vol. 41, no. 12, pp. 2881–2889, Dec. 2003.

[9] D. Hoekman, M. Vissers, and T. Tran, "Unsupervised full-polarimetric SAR data segmentation as a tool for classification of agricultural areas," *IEEE J. Sel. Topics Appl. Earth Observ. Remote Sens.*, vol. 4, no. 2, pp. 402–411, Jun. 2011.

[10] H. Skriver, "Crop classification by multitemporal C- and L-band single-and dual-polarization and fully polarimetric SAR," *IEEE Trans. Geosci. Remote Sens.*, vol. 50, no. 6, pp. 2138–2149, Jun. 2012.

[11] G. Anconitano, S.-B. Kim, B. Chapman, J. Martinez, P. Siqueira, and N. Pierdicca, "Classification of Crop Area Using PALSAR, Sentinel-1, and Planet Data for the NISAR Mission," *Remote Sens.*, vol. 16, no. 11, 2024, Art. no. 1975.

[12] S. Kraatz et al., "Comparison between Dense L-Band and C-band synthetic aperture radar (SAR) time series for crop area mapping over a NISAR calibration-validation site," *Agronomy*, vol. 11, no. 2, 2021, Art. no. 273.

[13] S. S. Ghosh et al., "Enhancing crop type classification from multifrequency dual-pol SAR data by probabilistic fusion of Gaussian processes," in *Proc. IEEE Int. Geosci. Remote Sens. Symp.*, 2024, pp. 8629–8632.

[14] S. Paloscia et al., "SAR multi-frequency observations of vegetation in agricultural and mountain areas," in *Proc. 33rd Gen. Assem. Sci. Symp. Int. Union Radio Sci.*, 2020, pp. 1–2.

[15] C. Gomez, J. C. White, and M. A. Wulder, "Optical remotely sensed time series data for land cover classification: A review," *ISPRS J. Photogrammetry Remote Sens.*, vol. 116, pp. 55–72, 2016.

[16] H. Skriver et al., "Crop classification using short-revisit multitemporal SAR data," *IEEE J. Sel. Topics Appl. Earth Observ. Remote Sens.*, vol. 4, no. 2, pp. 423–431, Jun. 2011.

[17] R. Sonobe, "Parcel-based crop classification using multi-temporal TerraSAR-X dual polarimetric data," *Remote Sens.*, vol. 11, no. 10, 2019, Art. no. 1148.

[18] M. Busquier, J. M. Lopez-Sanchez, and D. Bargiel, "Added value of coherent copolar polarimetry at X-band for crop-type mapping," *IEEE Geosci. Remote Sens. Lett.*, vol. 17, no. 5, pp. 819–823, May 2020.

[19] L. D. Robertson, A. Davidson, H. McNairn, M. Hosseini, and S. Mitchell, "Assessment of multi-frequency SAR for crop type classification and mapping," in *Proc. IEEE Int. Geosci. Remote Sens. Symp.*, 2019, pp. 489–492.

[20] H. McNairn, L. D. Robertson, D. Tsan, X. Jiao, and A. Davidson, "Multifrequency SAR to monitor agriculture in the Americas," in *Proc. IEEE Int. Geosci. Remote Sens. Symp. IGARSS*, 2021, pp. 5914–5916.

[21] F. Mattia et al., "Earth observation retrieval and classification algorithms for agriculture," in *Proc. IEEE Int. Geosci. Remote Sens. Symp.*, 2023, pp. 1428–1431.

[22] R. Bamler and P. Hartl, "Synthetic aperture radar interferometry," *Inverse Problems*, vol. 14, no. 4, pp. 1–54, 1998.

[23] T. Strozzi et al., "Landuse mapping with ERS SAR interferometry," *IEEE Trans. Geosci. Remote Sens.*, vol. 38, no. 2, pp. 766–775, Mar. 2000.

[24] M. Engdahl and J. Hyyppa, "Land-cover classification using multitemporal ERS-1/2 InSAR data," *IEEE Trans. Geosci. Remote Sens.*, vol. 41, no. 7, pp. 1620–1628, Jul. 2003.

[25] F. Sica, A. Pulella, M. Nannini, M. Pinheiro, and P. Rizzoli, "Repeat-pass SAR interferometry for land cover classification: A methodology using Sentinel-1 short-time-series," *Remote Sens. Environ.*, vol. 232, 2019, Art. no. 111277.

[26] A. W. Jacob et al., "Sentinel-1 InSAR coherence for land cover mapping: A comparison of multiple feature-based classifiers," *IEEE J. Sel. Topics Appl. Earth Observ. Remote Sens.*, vol. 13, pp. 535–552, 2020.

[27] A. Mestre-Quereda, J. M. Lopez-Sanchez, F. Vicente-Guijalba, A. W. Jacob, and M. E. Engdahl, "Time-series of Sentinel-1 interferometric coherence and backscatter for crop-type mapping," *IEEE J. Sel. Topics Appl. Earth Observ. Remote Sens.*, vol. 13, pp. 4070–4084, 2020.

[28] M. Busquier, J. M. Lopez-Sanchez, A. Mestre-Quereda, E. Navarro, M. P. Gonzalez-Dugo, and L. Mateos, "Exploring TanDEM-X interferometric products for crop-type mapping," *Remote Sens.*, vol. 12, no. 11, 2020, Art. no. 1774.

[29] S. Cloude and K. Papathanassiou, "Polarimetric SAR interferometry," *IEEE Trans. Geosci. Remote Sens.*, vol. 36, no. 5, pp. 1551–1565, Sep. 1998.

[30] N. Romero-Puig, J. M. Lopez-Sanchez, and M. Busquier, "Evaluation of PolInSAR observables for crop-type mapping using bistatic TanDEM-X data," *IEEE Geosci. Remote Sens. Lett.*, vol. 19, 2022, Art. no. 4508005.

[31] M. Busquier, J. M. Lopez-Sanchez, F. Ticconi, and N. Floury, "Combination of time series of L-, C-, and X-band SAR images for land cover and crop classification," *IEEE J. Sel. Topics Appl. Earth Observ. Remote Sens.*, vol. 15, pp. 8266–8286, 2022.

[32] R. Horn, A. Nottensteiner, A. Reigber, J. Fischer, and R. Scheiber, "F-SAR - DLR new multifrequency polarimetric airborne SAR," in *Proc. 2009 IEEE Int. Geosci. Remote Sens. Symp.*, 2009, vol. 2, pp. 902–905.

[33] S. R. Cloude, *Polarisation: Applications in Remote Sensing*. Oxford, UK.: Oxford Univ. Press, 2009.

[34] A. Marino, "Trace coherence: A new operator for polarimetric and interferometric SAR images," *IEEE Trans. Geosci. Remote Sens.*, vol. 55, no. 4, pp. 2326–2339, Apr. 2017.

[35] B. Tso and P. Mather, *Classification Methods for Remotely Sensed Data*, 2nd ed. Boca Raton, USA: CRC Press, 2001.

[36] S. Valero, L. Arnaud, M. Planells, E. Ceschia, and G. Dedieu, "Sentinel's classifier fusion system for seasonal crop mapping," in *Proc. IEEE Int. Geosci. Remote Sens. Symp.*, 2019, pp. 6243–6246.

[37] S. Valero, L. Arnaud, M. Planells, and E. Ceschia, "Synergy of Sentinel-1 and Sentinel-2 imagery for early seasonal agricultural crop mapping," *Remote Sens.*, vol. 13, no. 23, 2021, Art. no. 4891.

[38] L. Breiman, "Random Forests," *Mach. Learn.*, vol. 45, pp. 5–32, 2001.

[39] G. E. Hinton, "Training products of experts by minimizing contrastive divergence," *Neural Comput.*, vol. 14, no. 8, pp. 1771–1800, 2002.

[40] F. Pedregosa et al., "Scikit-learn: Machine learning in Python," *J. Mach. Learn. Res.*, vol. 12, pp. 2825–2830, 2011.

[41] S. V. Stehman, "Selecting and interpreting measures of thematic classification accuracy," *Remote Sens. Environ.*, vol. 62, no. 1, pp. 77–89, 1997.

[42] T. Di Martino, R. Guinvarc'h, L. Thirion-Lefevre, and E. Colin, "Beets or cotton? Blind extraction of fine agricultural classes using a convolutional autoencoder applied to temporal SAR signatures," *IEEE Trans. Geosci. Remote Sens.*, vol. 60, 2022, Art. no. 5212018.

[43] T. Di Martino, R. Guinvarc'h, L. Thirion-Lefevre, and E. Colin, "FARM-SAR: Fixing agricultural mislabels using Sentinel-1 time series and autoencoders," *Remote Sens.*, vol. 15, no. 1, 2023, Art. no. 35.

[44] A. Larrañaga and J. Álvarez Mozos, "On the added value of quad-pol data in a multi-temporal crop classification framework based on RADARSAT-2 imagery," *Remote Sens.*, vol. 8, no. 4, 2016, Art. no. 335.

[45] K. Stankiewicz, "The efficiency of crop recognition on ENVISAT ASAR images in two growing seasons," *IEEE Trans. Geosci. Remote Sens.*, vol. 44, no. 4, pp. 806–814, Apr. 2006.

Noelia Romero-Puig (Member, IEEE) received the B.Sc. degree in sound and image in telecommunication engineering, the M.Sc. degree in telecommunication engineering, and the Ph.D. degree in computer science from the University of Alicante, Alicante, Spain, in 2016, 2018, and 2021, respectively.

She was with the Signals, Systems, and Telecommunication Group, University of Alicante. Since January 2022, she has been a Postdoctoral Research Scientist with the Information Retrieval Group, Radar Concepts Department, Microwaves and Radar Institute, German Aerospace Center (DLR), enhofen, Wessling, Germany. Her research interests include polarimetric and interferometric synthetic aperture radar (PolSAR and PolInSAR) data processing and algorithm development for the retrieval of biophysical parameters over natural environments such as agricultural areas and forests.

Dr. Romero-Puig was the recipient of the IEEE GRSS Spanish Chapter Award for the Best M.Sc. Thesis in Remote Sensing defended in Spain in 2018, the Hisdesat Award for the Best M.Sc. Thesis in Government Satellite Services from the Official College of Telecommunications Engineers (COIT) in 2019, and the Ph.D. Special Award from the University of Alicante in 2025.

Mario Busquier was born in Elda, Spain, in 1994. He received the B.Sc. degree in sound and image in telecommunication engineering, the M.Sc. degree in telecommunication engineering, and the Ph.D. degree in computer science from the University of Alicante, Alicante, Spain, in 2018, 2020, and 2023, respectively.

He worked with the Signals, Systems and Telecommunications Group (SST), as a Predoctoral Researcher from 2019 to 2023. Since 2024, he has been with iABG mbH as a Radar Expert and has been involved in projects such as CEMS (Copernicus Emergency System) and LBM-DE (Landbedeckungsmodell fur Deutschland), among others, developing workflows for satellite imagery processing and classification. His main research interests include crop-type mapping by means of radar data, SAR polarimetry and interferometry, and development of scripts for automatic processing of time series of SAR SLC images.

Dr. Busquier was the recipient of the Award for Best Final Master thesis in Remote Sensing defended in Spain in 2020 of the IEEE GRSS Spanish Chapter and was also awarded in 2022 with the *Hall of Fame Award* by the Technical University of Alicante (EPS UA).

Jiayin Luo (Member, IEEE) was born in Liaoning, China, in 1995. She received the B.S. degree in geomatics engineering from the Northeastern University, Shenyang, China, in 2018, the M.S. degree in geomatics engineering from Wuhan University, Wuhan, China, in 2020, and the Ph.D. degree in computer science from the University of Alicante, Alicante, Spain, in 2024.

From 2020 to 2024, she worked as a Postdoctoral Researcher with the University of Alicante, Alicante, Spain. Since 2024, she has been a Lecturer with the College of Resources and Civil Engineering, Northeastern University, Shenyang, China. Her research interests include polarimetric and interferometric techniques.

Juan M. Lopez-Sanchez (Senior Member, IEEE) was born in Alicante, Spain, in 1972. He received the Ingeniero (M.S.) and Doctor Ingeniero (Ph.D.) degrees in telecommunication engineering from the Technical University of Valencia, Valencia, Spain, in 1996 and 2000, respectively.

From 1998 to 1999, he was a Predoctoral Grantholder with the Space Applications Institute, Joint Research Centre of the European Commission, Ispra, Italy. Since 2000, he leads the Signals, Systems and Telecommunication Group of the University of Alicante, Alicante, Spain, where he has been a Full Professor since November 2011. His research interests include microwave remote sensing for inversion of biophysical parameters, polarimetric and interferometric techniques, and applications of radar remote sensing in agriculture and geophysics.

He has coauthored more than 130 papers in refereed journals and more than 170 papers and presentations in international conferences and symposia. In 2001, Dr. Lopez-Sanchez received the Indra Award for the best Ph.D. thesis about radar in Spain. From 2006 to 2012 he was the Chair of the Spanish Chapter of the IEEE Geoscience and Remote Sensing Society.

Francesca Ticconi (Member, IEEE) received the Laurea degree in electronic engineering and the Ph.D. degree in electromagnetism from the University of Rome La Sapienza, Rome, Italy, in 2003 and 2007, respectively.

From July 2003 to October 2005, she was with the Italian Environmental Protection Agency (APAT), analyzing the development of new technologies suitable for minimizing electromagnetic emissions. After the Ph.D. degree, from November 2007 to September 2008, she was with the Centre of Terrestrial Carbon Dynamics (CTCD), University of Sheffield, Sheffield, U.K., where she worked on SAR image processing for forest monitoring. Until December 2010, she was with the German Aerospace Centre (DLR), where she studied scattering electromagnetic models for the interpretation of polarimetric and interferometric SAR data. Until May 2013, she was with the School of Earth and Environment, University of Leeds, Leeds, U.K., where her activity focused on measuring changes of glaciers and Greenland ice sheets by using radar altimetry. From June 2013 until January 2020, she was with the Remote Sensing and Product Division in EUMETSAT, where she worked within the scatterometry team on developing the processing algorithms for the product generation of the new EPS-SG scatterometer instrument. Since February 2020, she has been with ESA in the Wave Interaction and Propagation Section where she contributes to the performance assessment of several missions (i.e., BIOMASS, CIMR, and ROSE-L). She is also involved in modeling the effects of the ionosphere on polarimetric synthetic aperture radar (SAR) data and on a correction algorithm for their mitigation. Her research interests include the microwave interaction with natural media and in particular the wave scattering and propagation from the Earth's surface, for the estimation of bio-geophysical parameters. She is also interested in remote sensing of the oceans and the cryosphere.

Dr. Ticconi is Member of the IEEE Geoscience and Remote Sensing Society.

Irena Hajnsek (Fellow, IEEE) received the Dipl. degree (Hons.) in fluvial river systems from the Free University of Berlin, Berlin, Germany, in 1996, the Dr. rer. nat. degree (Hons.) in model-based estimation of soil moisture from fully polarimetric synthetic aperture radar from the Friedrich Schiller University of Jena, Jena, Germany, in 2001, and the Doctor degree honoris causa from the University of Oslo, Oslo, Norway.

Since November 2009, she has been a Professor of Earth Observation with the Swiss Federal Institute of Technology (ETH), Zurich Institute of Environmental Engineering, Zurich, Switzerland, and at the same time the Head of the Polarimetric SAR Interferometry Research Group, German Aerospace Center Microwaves and Radar Institute, Wessling, Germany. Since 2010, she has been with the Science Coordinator of German Satellite Mission TanDEM-X. Her research interests include electromagnetic propagation and scattering theory, radar polarimetry, SAR and interferometric SAR data processing techniques, and environmental parameter modeling and estimation.

Dr. Hajnsek was a Member of IEEE GRSS AdCom, from 2013 to 2021. She is a Member of European Space Agency Mission Advisory Group for the ROSE-L Mission. In 2024, she was awarded with the Doctor degree honoris causa by the University of Oslo for her outstanding contributions to science, including the development of algorithms using innovative radar techniques for environmental parameter estimation and setting requirements for the design of future radar missions in application areas as permafrost, glaciers, disaster management, agriculture, and climate change impacts. She was the Technical Program Co-Chair of the IEEE IGARSS 2012 in Munich, Germany, and 2019 in Yokohama, Japan. She was the Vice President of the IEEE GRSS Technical Committees, from 2016 to 2020. She has been the Founder of the New Technical Committee Remote Sensing Environment, Analysis and Climate Technologies (REACT), which exists, since November 2021.